Parametric Structural Design of Vertical-Axis Tidal Turbine Arrays

Anthony Clay

A thesis
submitted in partial fulfillment of the
requirements for the degree of

Master of Science

University of Washington

2023

Committee:
Michael Motley
Richard Wiebe
Brian Polagye

Program Authorized to Offer Degree:
Civil and Environmental Engineering

University of Washington

Abstract

Parametric Structural Design
of Vertical-Axis Tidal Turbine Arrays

Anthony Clay

Co-Chairs of the Supervisory Committee:
Michael Motley
Department of Civil and Environmental Engineering

Richard Wiebe
Department of Civil and Environmental Engineering

This thesis presents an approach for the structural design of vertical-axis tidal turbine arrays, including both the turbine blades and the supporting superstructure. Design load cases and performance goals are established in a Load and Resistance Factor Design (LRFD) framework. A simplified frame model is derived to efficiently perform a parametric study on blade structural performance using loads derived from hydrodynamic simulations. This model is compared to a higher resolution finite element model of the blade to identify ways in which the simplified model may underestimate stresses and deflections. A frame model is developed for the superstructure using loads derived from experimental hydrodynamic data. The design approach and component models are implemented in a parametric design algorithm which determines the required size of each structural component for a given set of flow, control, and geometric parameters. The parametric design algorithm is applied for a range of turbine conditions representative of potential sites and control strategies. Trends in the structural requirements, controlling limit states, and limits of feasibility are discussed.

TABLE OF CONTENTS

Page

LIST OF FIGURES

LIST OF TABLES

ACKNOWLEDGMENTS

Thank you to

- My advisors Michael Motley and Richard Wiebe, for their excellent guidance and encouragement throughout this project.
- Professor Brian Polagye, for being willing to discuss the minutiae of the structural design even while managing the big-picture aspects of this project.
- Professor Jen Franck, Mukul Dave, and Rithwik Kandukuri at the University of Wisconsin-Madison Department of Engineering Physics, for their contributions of CFD simulation data and collaboration on modeling of fluid-structure interactions.
- Aidan Hunt, for contributing experimental data on turbine force coefficients.
- Ben Terry, for writing the base of the superstructure parametric design code, and for starting me off in the right direction on this project.
- My friends and family for their infinite support and inspiration.

This work was supported by the US Department of Energy through Grant # DE-AR0001441

Chapter 1

INTRODUCTION

1.1 Motivation & Background

Tidal power shows promise as a relatively unexploited source of renewable energy. Tidal energy harvesting is at its most viable in narrow channels, which have a high enough density of kinetic energy in the flow to make extraction economically feasible. Due to the limited space in such channels, there is incentive to make tidal turbine farms as space-efficient as possible.

Similar to wind turbines, tidal turbines can be categorized by their orientation relative to the flow. Horizontal-axis tidal turbines (HATT), also known as axial-flow turbines, rotate about an axis parallel to the flow. Vertical-axis tidal turbines (VATT), also known as cross-flow turbines, rotate about an axis perpendicular to the flow. Dabiri [6] demonstrated that an array of counter-rotating vertical-axis wind turbines (VAWT) can achieve higher energy output per square meter than traditional wind farm designs, leading to interest in a similar concept for tidal turbines. Efficiency may be improved further by exploiting the effects of confined flow if the turbine array spans a significant fraction of a tidal channel [9].

This work is part of a larger project advancing the design of "Confinement-Exploiting Cross-Flow Turbine Arrays" (ConEXT), within ARPA-E's Submarine Hydrokinetic And Riverine Kilo-megawatt Systems (SHARKS) program. The ConEXT project employs a co-design framework to meet the many interdisciplinary needs of tidal turbine design, including experimental and numerical hydrodynamics, structural design, power electronics, environmental impact, and economic analyses. This thesis summarizes current progress in the structural design portion of the ConEXT project.

One goal of the project is to design the arrays such that they are *modular* and *con-*

tainerized; *modular* meaning that the array consists of identical components for simplicity of manufacturing, and *containerized* meaning that the components are sized to be transported within standard commercially available shipping containers. Within these constraints, the turbine array layout can be optimized for a given channel. The modular containerized array concept is depicted in Figure 1.1.

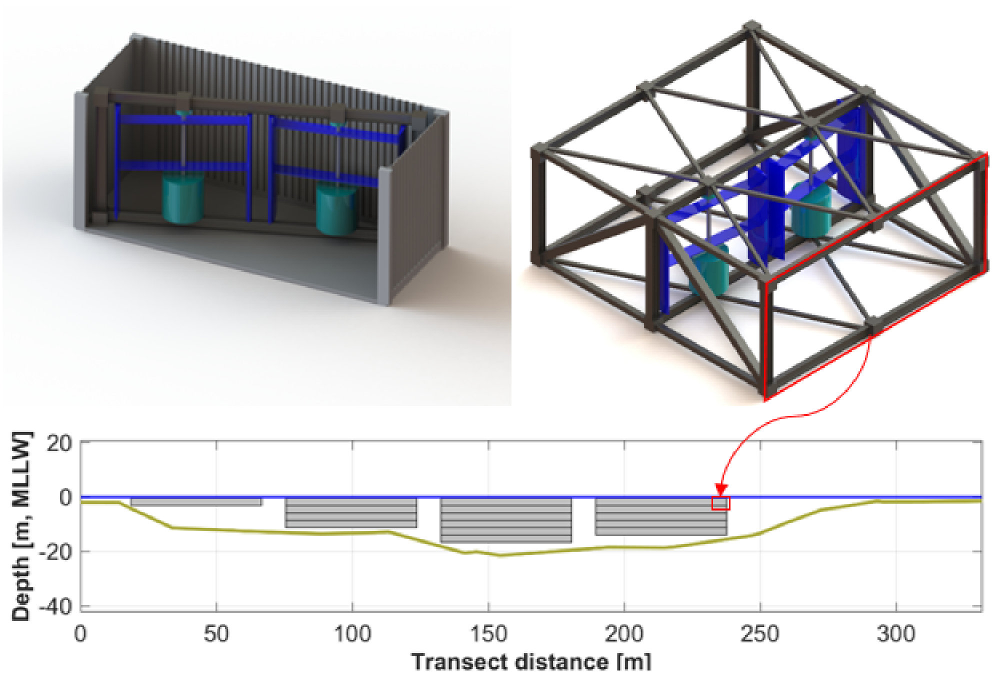

Figure 1.1: Modular containerized array concept. Top Left: turbines & superstructure frame in transport. Top Right: assembled turbine module. Bottom: Potential array layout at channel cross-section in Angoon, AK, USA. Conceptual drawings by Gemma Calandra, array layout by Brian Polagye

Tidal turbines introduce significant technical challenges when compared with wind turbines. Tidal currents see lower flow speeds than wind turbines, and are typically smaller than wind turbines of comparable power, but considering the higher density of water relative to air, the aggregate effect is still a significant increase in force experienced by the turbine [8]. While this is promising for power generation, it is more demanding of the structural design.

In the absence of an established design code, design of VATT can be informed by existing sources on horizontal-axis tidal turbines (HATT). These differ from VATT in their geometry, but face similar loading conditions. Thus, sources on HATT such as [4] and [8] can be referenced for guidance on load cases and material selection.

Turbine blades for both wind and tidal energy are commonly made with fiber-reinforced polymer composites, which have a high stiffness and strength relative to their weight. Glass fiber reinforced polymer (GFRP) is the most common material of choice for wind turbine blades, but the extreme load conditions experienced by tidal turbines may exceed the available strength of GFRP [10]. Carbon fiber reinforced polymer (CFRP) can have higher stiffness and strength, although it comes at higher expense.

The design space of a vertical-axis turbine array is vast, including site characteristics such as channel geometry and inflow velocity distribution, rotor characteristics such as blade length and preset pitch angle, and control parameters such as rated speed and control strategy. Finding the optimal set of design variables requires iteration over many points. Thus, it is important to have a consistent design framework which can identify the structural requirements of the array for any chosen set of design variables and parameters. This framework should be paired with analysis tools which can efficiently perform the required structural analyses so that the design space can be explored in a reasonable amount of time. There is a tradeoff between the computation time and the level of detail of analysis. For that reason this project prioritizes aspects of the design which are expected to drive the overall cost.

1.2 Scope

This thesis presents an approach for the structural design of vertical-axis tidal turbine arrays, specifically design issues related to composite blades and supporting steel superstructure. The approach is implemented in a parametric design algorithm which determines the required size of each structural component for a given set of flow and control parameters. The parametric design algorithm is then applied to a range of input parameters generated from experimental and simulated hydrodynamic data.

This work is far from an exhaustive overview of all aspects of the structural design of vertical-axis tidal turbines. Primary focus is given to the aspects of design which are expected to drive the cost associated with the structure, as these are of most importance to determining the economic viability of VATT arrays. Thus, details which do not significantly alter the required mass of CFRP or steel are not investigated in this work.

The manufacturing of the blades is not considered beyond the general concept of a wrapped box-spar design. This precludes any detailed design of connections, which must be informed by manufacturing choices. Although it is included in the design framework, no explicit fatigue analysis is conducted for the designs presented, as fatigue characteristics of carbon fiber can be highly dependent material properties and manufacturing details. Likewise, the connection details of the steel superstructure are not considered beyond "fixed" versus "pinned" connections (i.e. whether or not the connections should be designed to transfer bending moments), because they are not expected to significantly alter the total cost associated with the structural design.

This thesis does not seek to give definitive recommendations for how VATTs should be designed, which would be outside the expertise of the author. Instead, it is meant to provide insight into load cases and performance goals, methods of analysis, trends in the required structural sizes, and the limits of feasibility in the design space.

1.3 Overview

Chapter 2 discusses the structural design of the composite turbine blades. Load cases are defined based on service and extreme operating conditions. For each load case, performance goals are defined. A simplified frame model is derived to efficiently analyze the deformations and stresses in the blade. This model derives the structural stiffness matrix based on classical lamination theory. The simplified frame model is compared against a higher resolution finite element model of the blade to assess its validity. Natural frequencies are calculated based on the structural stiffness, damping, and mass matrices, with additional fluid terms based on

Theodorsen's unsteady foil theory. The design approach and frame model are implemented in a parametric design algorithm which determines the required composite laminate thickness of each component of the blade.

Chapter 3 discusses the design of the supporting superstructure in a similar approach to Chapter 2. Load cases are defined based on service and extreme operating conditions. For each load case, performance goals are defined. A frame element model is constructed using properties of available wide-flange steel sections. The design approach and frame model are implemented in a parametric design algorithm which determines the required wide-flange section for each member of the superstructure frame.

Chapter 4 applies the blade and superstructure parametric design algorithms over a range of flow and control parameters. Trends in the structural design, controlling load cases, and limits of feasibility are discussed.

Chapter 5 summarizes and interprets results of the parametric study, discusses implications for the design of vertical-axis tidal turbine arrays, and discusses avenues for further research.

Chapter 2

BLADE DESIGN

Prior to the structural design of the blades, parameters such as the turbine radius, number of blades, blade length, foil shape, chord length, and preset pitch angle are chosen based on hydrodynamic considerations. From this point, the goal of the structural design is to size the internal components of the blade and supporting structures to provide adequate stiffness and strength throughout the lifetime of the turbine. The design space of possible structural layouts and materials for the superstructure is extremely large, so reasonable constraints are used to narrow it down.

2.1 Material Selection

Although a range of materials were initially considered, carbon fiber was settled upon as the composite of choice for the spar and skin laminates. Fiberglass is commonly used for wind turbine blades, but the extreme loading conditions in most tidal energy extraction sites make it infeasible for this application. This conclusion was also reached by Grogan et al [10] in the design of composite blades for a HATT. A brief estimation of bending stresses in the blade demonstrates this infeasibility:

It is shown in Figure 2.8 that the design load normal to the blade under extreme conditions can be more than 350 kN/m. For a simply supported blade with a length of 2.15m, this leads to a bending moment of up to

$$M_{\text{max}} = \frac{w_T L^2}{8} \approx \frac{350\text{kN/m} \times (2.15\text{m})^2}{8} = 202\text{kN-m}$$

The moment of inertia of the blade is limited by the available space within the foil profile. The maximum rectangular spar that can fit within a 0.58m NACA0018 foil is approximately

Property	ρ	$\mathbf{E_1}$	$\mathbf{E_2}$	$\mathbf{G_{12}}$	$\nu_{\mathbf{12}}$	$\nu_{\mathbf{23}}$
Design Value	$1.6\frac{g}{cm^3}$	$138 \times 10^9\mathrm{Nm}^2$	$11 \times 10^9\mathrm{Nm}^2$	$5.5 \times 10^9\mathrm{Nm}^2$	.28	.4

Property	$\mathbf{S_1^+}$	$\mathbf{S_1^-}$	$\mathbf{S_2^+}$	$\mathbf{S_2^-}$	$\mathbf{S_{12}}$	
Design Value	1500MPa	900MPa	27MPa	200MPa	100MPa	

Table 2.1: Design properties of T300/914-C CFRP plies used in this study. ρ is the density. E_1, E_2, and G_{12} are the elastic & shear moduli. ν_{12} and ν_{23} are the in-plane and out-of plane Poisson ratios. S_1^+, etc. are the failure stresses in each orthotropy direction in tension (+), compression (-), and shear. Source: [3]

28cm x 8cm. Assuming a fully solid spar (which is an overestimate), the moment of inertia would be

$$I \leq \frac{bh^3}{12} \approx \frac{.28\mathrm{m} \times (.08\mathrm{m})^3}{12} = 1.2 \times 10^{-5}\mathrm{m}^4$$

with a maximum distance of $y = 0.04$ m from the neutral axis. The maximum bending stress in the spar would be

$$\sigma_{\max} = \frac{My}{I} \approx \frac{202\mathrm{kN\text{-}m} \times .04\mathrm{m}}{1.2 \times 10^{-5}\mathrm{m}^4} = 674\mathrm{MPa}$$

which exceeds the compressive strength of most GFRP composites. Since the moment of inertia I will likely be less than that of a solid spar, the stress will only be higher than that predicted above. Thus, GFRP is not considered viable for this application. Instead, CFRP is assumed for the blades. Table 2.1 shows the material properties assumed for CFRP in this study. Although this work will focus on CFRP composites, the same design approach could be used for GFRP blades if the conditions were appropriate. It may be feasible to use a CFRP for the main spar to give sufficient bending strength, but GFRP for the skin, which does not need to transfer as much load.

2.2 Structural Layout

A wrapped box-spar design was chosen for the blades. This design consists of a rectangular spar running along the length of the blade, wrapped in a thinner skin which gives the blade its hydrofoil shape and transfers loads from the fluid to the spar. This skin can be connected to the spar via supporting ribs, or via a structural foam infill. The spar is supported at two points by struts, which may be continuously connected to into the spar wall. Together, the blade and supporting struts are referred to as the “blade assembly”, shown in Figure 2.1.

Note that although Figure 2.1 shows the supporting struts at the ends of the blade, they may instead be placed along the span, both to provide a more efficient structural configuration and to make room for power generation equipment at the base of the rotor. The chosen structural configuration is intended to provide an estimate of the structural material required, and not necessarily as a recommendation for structural detailing. Other configurations, such as a scenario where the skin is used as the primary structural element, are expected to be slightly more efficient because the skin is slightly further from the neutral axis, but these designs come with other detailing challenges such as stress concentrations at the trailing edge.

This design has the advantage that the main spar and skin may be sized nearly independently of the other components, which is suitable for parametric design. The spar is designed to carry the entirety of the bending moment demand by itself. For torsional moment, both the spar and the skin contributions to stiffness are included. This box-spar design is used for purposes of cost estimation, assuming that the total material cost will be similar to that of other designs (e.g., spar cap & shear web designs). This is justified by the fact that the spar materials are largely located near the extreme compression and tension fibers of the blade cross-section, and thus deliver a reasonably efficient structural configuration.

2.3 Proposed Design Framework

A load & resistance factor design approach (LRFD) was used to design the blades, patterned after ASCE standards used in design of civil structures [2]. LRFD achieves a reliable design by applying factors to increase the design load and decrease the design strength of the structure. If calculations indicate that the structure will not fail under the increased load and reduced strength, then it should have a low probability of failure under actual conditions.

The load factor (denoted γ) may vary for each load case, and the resistance factor (denoted ϕ) may vary for each type of structural failure being considered. For example, the load factor may be greater for load cases in which the load magnitude is more variable, and the resistance factor may be smaller for failure modes which are of higher consequence. In the absence of established factors for marine turbine design, this work makes reasonable assumptions to estimate design requirements. Two load cases are identified, corresponding to the normal operating conditions of the turbine and the likely most extreme operating conditions.

The operating conditions of the turbine are defined by two parameters: the freestream velocity, U_0, and the "tip speed ratio" (TSR), defined as $\lambda = \frac{\omega R}{U_0}$, where ω is the rotational rate of the turbine and R is the radius. The nominal current speed is identified from current speed measurements taken at a proposed site. The nominal TSR is chosen to optimize hydrodynamic performance based on experimental and simulated hydrodynamic data. Both U_0 and λ are treated as inputs to the structural design.

The most extreme load conditions to be encountered by the turbine were identified to occur in the *freewheel* operational condition. Normally, generator applies some amount of torque to the rotor to maintain optimal TSR and extract energy. Under some conditions, this control torque may not be applied, either deliberately to avoid overloading the power generation system in high-flow conditions, or as a result of failure of the turbine control system. In this case, the rotor will accelerate until all of the power being transferred into blades is dissipated by hydrodynamic losses, which we refer to as "freewheeling". The TSR at which freewheel occurs, denoted λ_{fw}, can be identified as the TSR at which the turbine coefficient of power crosses zero (shown in Figure 2.2). A load factor of 1.3 is applied to the nominal current speed at extreme load conditions to account for turbulent fluctuations. This factor is equal to the turbulence intensity factor, which is determined for a given site based on hydrodynamic analysis outside the scope of this paper.

Under extreme load conditions, the blades must not experience material failure. For this study material failure is defined using a maximum-stress failure criterion, described in Section 2.4. Additionally, the blade must remain stable. This is defined using stability criteria for vertical-axis turbines derived in [15]. These stability criteria include torsional divergence, centrifugal buckling, and main resonance, and are discussed in Section 2.6.1.

Service load conditions are defined to occur with the turbine operating at nominal TSR and current speed. Under service load conditions, all performance goals of the extreme load condition apply, with the additional goals of limiting structural deformations such that the hydrodynamic performance of the turbine is not significantly affected, and limiting stresses such that the blade does not experience fatigue failure within its design lifetime. As it is not yet known exactly how far the blade may deform before the hydrodynamics are significantly altered, placeholder values of $\delta_{\max} < 0.03L$ and $\Delta\alpha_{\max} < 1^\circ$ are used in this study to limit the normal and twisting deformations, respectively. Designing for the fatigue limit state is not considered in this study, but it is included in the design framework for completeness.

The above load cases are selected to conservatively overestimate the loading on the blade. Likewise, a strength reduction factor is applied to conservatively underestimate the strength of the blade. This factor, denoted ϕ, is set to 0.75 for the ultimate load case, matching the limit used for fracture-critical structures in LRFD. For service loads, ϕ may be reduced to limit cyclic stresses which may cause fatigue failure.

In both load cases, the blade is analyzed using quasi-static loads. However, dynamic effects may play a significant role due to the cyclic nature of the blade loading. To account for this, an additional constraint is added that the dynamic amplification factor (DAF), defined in Equation (2.1), must be less than 1.05. The dynamic amplification factor is greatest when the natural resonant frequency of the structure, ω_n, is equal to the frequency of excitation, ω (equal to the rotation rate). Conservatively assuming no damping, the expression can be simplified to the far right side of Equation (2.1):

$$\text{DAF} = \frac{1}{\sqrt{[1-(\omega/\omega_n)^2]^2 + [2\xi\omega/\omega_n]^2}} \underset{\xi\to 0}{=} \frac{1}{1-(\omega/\omega_n)^2} \tag{2.1}$$

Using this expression, the constraint of DAF $\leq$ 1.05 becomes equivalent to $\omega_n/\omega \geq 4.5$ (reasonably assuming that the structural frequency is not less than the rotational frequency). The structural frequency ω_n is calculated in Section 2.6.

Load cases and performance goals of the blade design are summarized in Table 2.3.

2.4 Simplified Frame Model

In order to effectively explore the design space of the turbines, it is necessary to be able to rapidly calculate the blade structural requirements for given input parameters. The computation of minimum structural requirements is a problem of structural optimization which requires an iterative design process, also underscoring the need for fast structural analysis. It would be inefficient to perform a fully detailed 3D finite-element analysis for every candidate design at every combination of input variables. Instead, a simplified model was constructed to more quickly evaluate the structural requirements for given load conditions. This simplified model idealizes the blade and supporting struts as one-dimensional frame elements. For validation purposes, a more detailed 3D finite-element analysis using shell elements is performed for a controlling design case in Section 2.5.

Figure 2.4 shows the simplified geometry of the frame model with associated geometric parameters. R is the radius of the turbine, L is the length of the blade, and S_1 and S_2 are parameters which control the location of the supporting struts. R and L are limited based on the available space in the modular array concept; S_1 and S_2 are limited by the size and location of the generator. Having a larger span between the supporting struts will generally result in higher bending moment demands on the blade. To conservatively estimate the blade structural requirements before the generator size is known, the struts are assumed to

Table 2.2: Blade load cases and performance criteria

Load Case	**Conditions**	**Performance Criteria**
Service	Normal Operation • $U = U_{\text{site}}$ • $\lambda = \lambda_{\text{oper}}$	• Blade does not fracture • Blade remains stable • Deformations do not significantly affect performance • Stress below fatigue limit[a]
Ultimate	Freewheel • $U = 1.3 * U_{\text{site}}$ • $\lambda = \lambda_{\text{fw}}$	• Blade does not fracture • Blade remains stable

[a] not considered in this study

be placed at the ends of the blade, i.e. $S_1 = 0$, $S_2 = L$, however the parametric design code allows for arbitrary placement of struts.

To idealize the blade as a frame element, representative bending and twisting stiffnesses must be calculated. Here it is assumed that the majority of the blade's bending stiffness comes from the box-spar, with the skin and infill materials contributing relatively little to the bending stiffness. For torsion, it is assumed that the skin does contribute torsional stiffness, as it has more material further from the center of twist. The validity of these assumptions is discussed in Section 4.1.

Analytical expressions for the stiffnesses of a composite box-beam with an orthotropic laminate are derived from classical lamination theory following Chapter 6 of [14]. First, the ply stiffness matrix Q must be computed for each ply in the composite layup:

$$Q = \begin{bmatrix} \frac{E_1}{D} & \frac{\nu_{12}E_2}{D} & 0 \\ \frac{\nu_{12}E_2}{D} & \frac{E_2}{D} & 0 \\ 0 & 0 & G_{12} \end{bmatrix}$$

where Q relates the stresses and strains in a ply's orthotropy directions. This is transformed to the laminate coordinates via the matrices T_σ and T_ϵ:

$$\bar{Q} = T_\sigma^{-1} Q T_\epsilon$$

where

$$\begin{aligned} T_\sigma &= \begin{bmatrix} \cos^2(\theta) & \sin^2(\theta) & 2\cos(\theta)\sin(\theta) \\ \sin^2(\theta) & \cos^2(\theta) & -2\cos(\theta)\sin(\theta) \\ -\cos(\theta)\sin(\theta) & \cos(\theta)\sin(\theta) & \cos^2(\theta)-\sin^2(\theta) \end{bmatrix} \\ T_\epsilon &= \begin{bmatrix} \cos^2(\theta) & \sin^2(\theta) & \cos(\theta)\sin(\theta) \\ \sin^2(\theta) & \cos^2(\theta) & -\cos(\theta)\sin(\theta) \\ -2\cos(\theta)\sin(\theta) & 2\cos(\theta)\sin(\theta) & \cos^2(\theta)-\sin^2(\theta) \end{bmatrix} \end{aligned} \tag{2.2}$$

and θ is the angle between the ply orthotropy directions and the laminate reference coordinates. The ply stiffness matrices are combined in a weighted sum to get the laminate bending stiffness matrix, which relates the applied forces and moments per unit span (on the left) to the midplane strains and curvatures of a laminate (on the right):

$$\begin{Bmatrix} N_x \\ N_y \\ N_{xy} \\ M_x \\ M_y \\ M_{xy} \end{Bmatrix} = \begin{bmatrix} A_{3\times 3} & B_{3\times 3} \\ & \\ B^{\top}_{3\times 3} & D_{3\times 3} \end{bmatrix} \begin{Bmatrix} \epsilon_x^0 \\ \epsilon_y^0 \\ \gamma_{xy}^0 \\ \kappa_x \\ \kappa_y \\ \kappa_{xy} \end{Bmatrix} \tag{2.3}$$

where A, B, and D are 3x3 matrices calculated using Equation 3.20 from [14], reproduced below:

$$\begin{aligned} A_{ij} &= \sum_{k=1}^{K} (\bar{Q}_{ij})_k (z_k - z_{k-1}) \\ B_{ij} &= \frac{1}{2} \sum_{k=1}^{K} (\bar{Q}_{ij})_k (z_k^2 - z_{k-1}^2) \\ D_{ij} &= \frac{1}{3} \sum_{k=1}^{K} (\bar{Q}_{ij})_k (z_k^3 - z_{k-1}^3) \end{aligned} \tag{2.4}$$

This stiffness matrix is inverted to get the laminate compliance matrix:

$$\begin{Bmatrix} \epsilon_x^0 \\ \epsilon_y^0 \\ \gamma_{xy}^0 \\ \kappa_x \\ \kappa_y \\ \kappa_{xy} \end{Bmatrix} = \begin{bmatrix} \alpha_{3\times 3} & \beta_{3\times 3} \\ & \\ \beta^{\top}_{3\times 3} & \delta_{3\times 3} \end{bmatrix} \begin{Bmatrix} N_x \\ N_y \\ N_{xy} \\ M_x \\ M_y \\ M_{xy} \end{Bmatrix} \tag{2.5}$$

Finally, Euler-Bernoulli beam theory can be used to derive the following expressions for a box-beam's axial, bending, and twisting stiffnesses, found in Table A.3 of [14]:

$$
\begin{aligned}
\widehat{EA} &= \frac{2b_f}{(\hat{\alpha}_{11})_f} + \frac{2b_w}{(\hat{\alpha}_{11})_w} \\
\widehat{EI}_s &= \frac{b_f d_w^2}{2(\alpha_{11})_f} + \frac{2b_f}{(\delta_{11})_f} + \frac{2b_w^3}{12(\alpha_{11})_w} \\
\widehat{EI}_t &= \frac{b_w d_f^2}{2(\alpha_{11})_w} + \frac{2b_w}{(\delta_{11})_w} + \frac{2b_f^3}{12(\alpha_{11})_f} \\
\widehat{GJ} &= \frac{2d_f^2 d_w^2}{(\alpha_{66}^{\nu})_f d_f + (\alpha_{66}^{\nu})_w d_w}
\end{aligned}
\tag{2.6}
$$

where $\widehat{EA}$, $\widehat{EI}_s$, $\widehat{EI}_t$, and $\widehat{GJ}$ are the representative axial stiffness, s-axis bending stiffness, t-axis bending stiffness, and torsional stiffness respectively. The beams s- and t-axes are defined in Figure 2.7. The compliances α and δ represent submatrices of the laminate's compliance matrix, shown in Equation (2.5), evaluated at the laminate's neutral plane.

The parameters $\hat{\alpha}_{11}$ and α_{66}^{ν} are defined as follows:

$$\hat{\alpha}_{11} = \alpha_{11} - \frac{\beta_{12}^2}{\delta_{22}}$$

$$\alpha_{66}^{\nu} = \alpha_{66} - \frac{\beta_{66}^2}{\delta_{66}}$$

The geometric parameters shown in Figure 2.5 are not independent: if c and d_{tot} are known, then b_f is constrained by the foil geometry. Similarly, d and d_f can be determined from b_w, b_f, and t. The chord length c is set by blade power performance considerations. The parameter d_{tot} can therefore be varied to optimize the bending or torsional stiffness of the spar. Figure 2.6 shows the variation of bending stiffness versus the aspect ratio of a box-spar with 6mm wall thickness sized to fit within a NACA0018 foil with a chord length of 0.58m.

The optimal value of d_{tot} is independent of the spar thickness t. This means the optimal spar aspect ratio can be calculated once and held constant throughout the design process. Thus, the thickness t is the only remaining independent parameter, which is chosen using an iterative process, described in Section 2.13.

The supporting struts are analyzed as a flat laminated plate, sized to provide adequate stiffness and strength with minimal profile. As in the spar, the strut laminate was designed using unidirectional CFRP, to maximize bending stiffness. The width of the plate is set to match the width of the box-spar, to simplify the connection design. Thus, as in the spar, the strut thickness is the only independent variable, and is sized in the iterative algorithm described in Section 2.13. The bending and torsional stiffnesses of the strut can be calculated from classical lamination theory, yielding the equations

$$\begin{aligned} \widehat{EA} &= \frac{b_f}{\alpha_{11}} \\ \widehat{EI_s} &= \frac{b_f}{\delta_{11}} \\ \widehat{EI_t} &= \frac{b_f^3}{12\alpha_{11}} \\ \widehat{GJ} &= 4\frac{b_f}{\delta_{66}} \end{aligned} \tag{2.7}$$

2.4.1 Blade Loads

The sizing of the blade assembly begins with the calculation of loads. Because the blade is subject to effects including dynamic stall, wake interactions, and blockage effects, these cannot be easily calculated. Experimental data giving the total force on the rotor was available (and is used to design the superstructure in Chapter 3), but blade-level forces were not measured, necessitating the use of CFD.

For given design values of current speed (U_0) and tip speed ratio (λ), the loading on the blade is calculated based on RANS simulations performed by Dave et al [7]. At each timestep the pressure distribution around the blade is integrated to get nondimensional force coefficients in the streamwise (C_{Fx}) and cross-stream (C_{Fy}) directions. These phase-averaged values are dimensionalized as:

$$
\begin{aligned}
F_x &= C_{Fx} * \frac{1}{2}\rho U_0^2 A \\
F_y &= C_{Fy} * \frac{1}{2}\rho U_0^2 A
\end{aligned}
\tag{2.8}
$$

where ρ is the fluid density and $A = 2RL$ is the swept area of the turbine. This gives the net force on the blade in the x-y coordinate system, which is then transformed into chord-referenced tangential (t) and normal (s) components:

$$
\begin{aligned}
F_t &= F_x \cos(\theta - \alpha) + F_y \sin(\theta - \alpha) \\
F_s &= -F_x \sin(\theta - \alpha) + F_y \cos(\theta - \alpha)
\end{aligned}
\tag{2.9}
$$

where θ and α are defined as in Figure 2.7. The azimuthal positions with largest chord-referenced tangential and normal components are identified. These maximum net tangential and normal forces are divided by the blade length, giving a uniform distributed load magnitude, plotted in Figure 2.8. A torsional moment is also applied to the blade based on the eccentricity between the center of lift and the shear center of the blade. It is assumed that the force is applied at the theoretical center of lift located at the 1/4-chord point, and the shear center of the blade lies at the centroid of the spar.

2.4.2 Blade Stresses

Once the stiffness and loading on each component is calculated, the system is discretized and solved for displacements. Figure 2.9 shows a sample displaced shape after loads are applied.

Once the frame element axial force, shear force, bending moment, and torsion demands are known, the stress state in the spar flange can be calculated. First, the demands are converted to equivalent forces-per-length (N_ξ,N_η,$N_{\xi\eta}$) and moments-per-length (M_ξ,M_η,$M_{\xi\eta}$) in the flange using Equation 2.10.

$$\begin{aligned} N_{\xi,f} &= \frac{Ax}{2b_f + 2d_{tot}} + \frac{M_t(d/2)}{\widehat{EI}_s \alpha_{11}} \\ M_{\xi,f} &= \frac{M_t}{\widehat{EI}_s \delta_{11}} \\ N_{\xi\eta,f} &= \frac{T}{2dd_f} + \frac{V_t Q}{\widehat{EI}_t} \end{aligned} \tag{2.10}$$

These forces give the flange midplane strains and curvatures via the laminate's compliance matrix, shown in Equation 2.11.

$$\epsilon_0 = \left\{ \begin{array}{c} \alpha_{11} N_\xi \\ \\ \alpha_{12} N_\xi \\ \\ (\alpha_{33} - \frac{\beta_{33}^2}{\delta_{33}}) N_{\xi\eta} \end{array} \right\} \qquad \kappa = \left\{ \begin{array}{c} \delta_{11} M_\xi \\ \\ \delta_{12} M_\xi \\ \\ 0 \end{array} \right\} \tag{2.11}$$

From these we can calculate the strains in a ply at distance z from the laminate's neutral axis as

$$\epsilon = \epsilon_0 + \kappa z \tag{2.12}$$

And the stress state in that ply

$$\sigma' = Q T_\epsilon \epsilon \tag{2.13}$$

where σ' denotes the stresses in a given ply's orthotropy directions and Q and T_ϵ are defined above. Failure of the composite was predicted using a simple maximum-stress failure criterion, shown in Equation (2.14). If any stress component in a ply exceeds the corresponding compressive or tensile failure strength (shown in Table 2.1), the laminate is considered to have failed.

$$F = \max\left[\frac{\sigma_1}{S_1^+}, \frac{\sigma_1}{S_1^-}, \frac{\sigma_2}{S_2^+}, \frac{\sigma_2}{S_2^-}, \frac{\sigma_{12}}{S_{12}}\right] < 1 \tag{2.14}$$

The skin is designed using a quasi-isotropic CFRP laminate, sized to transfer load from the water to the spar. Assuming a rib-type connection between the skin and the spar, the skin must be sized for the maximum bending moment over the span between ribs. The largest unsupported span of the skin occurs between the spar and the trailing edge. The maximum bending moment can be estimated using the Navier solution to the Kirchoff-Love equations for bending of a simply supported rectangular plate:

$$M_x = \frac{16q}{\pi^4} \sum_{m=1,3,...}^{\infty} \sum_{n=1,3,...}^{\infty} \frac{\frac{m^2}{a^2} + \nu\frac{m^2}{b^2}}{mn(\frac{m^2}{a^2} + \frac{m^2}{b^2})} \sin(\frac{m\pi x}{a}) \sin(\frac{n\pi y}{b}) \tag{2.15}$$

where a and b are length and width of the plate, q is the applied uniform distributed load, and ν is the material Poisson ratio, calculated for the quasi-isotropic laminate using Equation (3.46) in [14]. Once the bending moment is known, the stress in the skin can be calculated using Equation (2.13) and evaluated using the maximum stress failure criterion.

The models for the spar, strut, and skin are applied in a parametric design algorithm in Section 2.7, after a brief detour to compare with a higher-fidelity model in Section 2.5 and investigate its dynamic characteristics in Section 2.6.

2.5 Shell Finite Element Model

A more high-fidelity finite element model (FEM) was developed to assess the validity of several assumptions inherent in the simplified frame model. This model is implemented in Abaqus, a commercial finite element analysis environment. The geometry of the FEM is shown in Figure 2.10. All components are meshed using 8-node rectangular shell elements.

Modeling the interaction between the spar and the skin is challenging due to the edge-surface interface between shell elements. A series of evenly spaced rigid ribs are placed between the skin and the spar. These ribs are modeled as shell elements with an extremely high membrane stiffness so that the pressure load is transferred directly from the skin to the spar. However, the ribs or infill are not expected to transfer shear loads between the spar and skin. To account for this, the bending stiffness components of the shell's stiffness matrix are artificially lowered to near zero, just large enough to avoid singularities in the stiffness matrix. Additionally, the corners of the spar are filleted and the ribs truncated so as not to directly connect the spar to the skin. These modifications are used for simulation purposes and are not representative of actual structural detailing. The resulting cross section is shown in Figure 2.1.

Details of the connection between the spar and struts can have a significant effect on the local distribution of stresses. However, this work is more concerned with the estimating the total material requirements, and exact details of the connections will not be determined until a later stage of design. For this model the connection is assumed to be a smooth transition between the flanges of the spar and the end of the strut, and analysis is primarily focused on the stresses far away from the connections.

In the frame model, the connection between the struts and central shaft is modeled as a fixed connection in the out-of-plane direction and a pin connection in the in-plane direction. This can be modeled in the FEM by pinning all the nodes at the boundary of the strut, with the out-of-plane fixity being provided by the reactions in the longitudinal direction. To avoid undue stresses from the Poisson effect, only a single node is pinned in the transverse direction, with the rest free to deform transversely.

The frame model applies hydrodynamic loads as a uniform distributed line load applied at the quarter-chord of the foil. However, the fully resolved two-dimensional pressure distribution over the foil was available from the University of Wisconsin-Madison RANS data. Two pressure distributions are selected for use in the FEM, corresponding to the phases of peak tangential force at operational and freewheel tip speed ratios. The pressure distributions are converted to distributed loads using Abaqus' "mapped analytical field" tool.

Figure 2.11 shows the selected pressure distributions along with the relative magnitude and direction of their resultant distributed loads. It can be seen that the location of the center of pressure for the blades is not at the theoretical 1/4-chord point, as assumed in the simplified frame model. The exact location of the center of pressure varies with the blade position, but appears to be closer to mid-chord at the location of peak tangential force. This means that the frame model conservatively overpredicts the maximum torsional demand on the blade, which is appropriate in the absence of a more detailed understanding of the variation of the center of pressure.

The resulting stresses and deflections calculated using the FEM are compared with the stresses and deflections predicted by the simplified frame model in Section 4.1.

2.6 Dynamic Characteristics

Up until this point, all calculations of deflection and stress have been quasi-static, neglecting any dynamic effects. However, dynamic effects are of concern due to the cyclic nature of the turbine loading. Resonance may occur if the frequency of the applied loading is at or near a natural resonant frequency of the structure. These natural frequencies can be calculated from the mass and stiffness properties of the blade assembly. The equation of motion for a structure in free vibration is

$$[M]\ddot{u}(t) + [C]\dot{u}(t) + [K]u(t) = 0 \tag{2.16}$$

where $[M]$, $[C]$, and $[K]$ are the structural mass, damping, and stiffness matrices, respectively, and u is the vector of nodal displacements. The stiffness matrix $[K]$ is calculated as in Section 2.9. The mass matrix $[M]$ is calculated based on the density of each component using a consistent-mass formulation. The damping matrix $[C]$ is estimated using a classical Rayleigh damping approach. This approach assumes that the damping matrix can be represented as a linear combination of the stiffness and mass matrices. The coefficients are determined by assigning a damping ratio to two chosen modes, which then determines the damping ratio for all modes. For this study, a damping ratio of 1% was assigned to the first and last modes. The linear differential equation shown in Equation 2.16 has solutions of the form

$$u(t) = \phi e^{\lambda t}$$

leading to the quadratic eigenvalue problem

$$(M\lambda^2 + C\lambda + K)\phi = 0$$

This problem can be solved for eigenvalues λ and eigenvectors ϕ using the approach described in [11]. For this study, MATLAB's `polyeig()` function is used to solve the quadratic eigenvalue problem. The solution consists of complex conjugate pairs of eigenvalues. The real part of these eigenvalues can be interpreted as a measure of damping, while the imaginary part gives a frequency of vibration (denoted ω_n). Any eigenvalue having $\text{Re}(\lambda) > 0$ corresponds to an unstable mode which will grow exponentially.

This approach predicts the natural frequencies and mode shapes of the structure in air, but does not account for the effects of the fluid flow around the blades. [5] proposed a model for the fluid effects on the structural dynamics hydrofoil in a water based on Theodorsen's unsteady foil theory. This theory is derived from linear potential flow theory and is typically applied in the aerospace field to predict the flutter frequency of aircraft wings. Although hydrofoils in water do not perfectly match the assumptions used to derive this theory, [5] investigated its potential to predict hydroelastic instabilities, comparing the model with experimental results. Although they concluded that the linear potential theory is not perfectly in agreement with experiments, and proposed improvements, the model should be sufficient for our purposes of estimating design requirements.

As the blade pitches and translates relative to the flow, the forces applied by the fluid are altered. The model accounts for these forces by adding the following equivalent mass, damping, and stiffness terms:

$$([M] + [M_f])\{\ddot{x}\} + ([C] + [C_f])\{\dot{x}\} + ([K] + [K_f])\{x\} = \{F\}$$

where

$$\{x\} = \left\{ \begin{array}{c} v \\ \\ \Delta\alpha \end{array} \right\}$$

contains the lifting (v) and pitching ($\Delta\alpha$) deformations and $[M_f]$, $[C_f]$, and $[K_f]$ are the fluid equivalent mass, damping, and stiffness terms, defined as

$$[M_f] = \pi b^2 \rho_f \begin{bmatrix} 1 & -ab \\ \\ -ab & (\frac{1}{8} + a^2)b^2 \end{bmatrix}$$

$$[C_f] = 2\pi b \rho_f U_n \begin{bmatrix} \mathrm{C}(k) & \frac{b}{2} + b(\frac{1}{2} - a)\mathrm{C}(k) \\ \\ -ec\mathrm{C}(k) & \frac{b^2}{2}(\frac{1}{2} - a) - ecb(\frac{1}{2} - a)\mathrm{C}(k) \end{bmatrix} \tag{2.17}$$

$$[K_f] = 2\pi b \rho_f U_n^2 \begin{bmatrix} 0 & \mathrm{C}(k) \\ \\ 0 & -ec\mathrm{C}(k) \end{bmatrix}$$

where b is the semichord length ($=\frac{c}{2}$), ab is the distance between midchord and the shear center, and ec is the distance between the aerodynamic and shear centers. These matrices are added into the global stiffness matrices at degrees of freedom corresponding to lifting and pitching deformations only. The geometric parameters used in Equation 2.17 are shown in Figure 2.12. Note that in the configuration show, ab has a negative value, because the shear center (referred to as the "elastic axis" in other works) is in front of the semichord.

$\mathrm{C}(k)$ is Theodorsen's circulation function applied to the reduced frequency $k = \frac{\omega_n b}{U_n}$. Thus, the calculation of the fluid terms requires the oscillating frequency ω_n as an input, and therefore must be calculated using an iterative process starting from an initial guess. In this study, the initial guess for ω_n is set equal to the pure structural frequency without fluid effects and then iterated upon using the Golden Search Method.

Results of the modal analysis are discussed in Section 4.2.1. The model described above is not directly implemented in the parametric design because the necessary iteration and repeated solving of the polynomial eigenvalue problem is computationally expensive. Instead, the above model is used to investigate limits imposed by dynamic requirements and to validate the use of a simpler closed-form equation to estimate ω_n, described in Section 2.7.

2.6.1 Instabilities

Terry et al. [15] investigated five forms of instability which may affect vertical-axis turbines. Of those instabilities, three are considered in this work: main resonance, torsional divergence, and centrifugal buckling. Main resonance is considered in the previous section, occuring when the natural frequency of the blade assembly coincides with the frequency of excitation. Torsional divergence occurs when the net flow speed on the blade is fast enough that small twisting deformations result in an increased pitching moment that overcomes structural restoring forces. Centrifugal buckling occurs when the turbine rotation is fast enough that small bending deformations lead to an increased centrifugal load that overcomes structural restoring forces. The following closed-form expressions were derived in [15] to predict the torsional divergence and centrifugal buckling of a vertical-axis tidal turbine:

$$U_d = C_\phi \sqrt{\frac{GJ}{\pi \rho_f e c^2 L^2}} \tag{2.18}$$

$$\Omega_c = C_\nu \sqrt{\frac{EI}{\rho_s A L^4}} \tag{2.19}$$

where U_d is the net current speed at which divergence occurs, Ω_c is the rotational frequency at which centrifugal buckling occurs, and C_ϕ and C_ν are constants determined from boundary conditions. For a blade with both ends fully fixed, [15] showed that $C_\phi = \pi$ and $C_\nu \approx 22.2$. Section 4.2.2 evaluates the above expressions for a sample design.

2.7 Parametric Design Algorithm

The components of the blade assembly were sized to satisfy all of the above design criteria using an iterative process. First, the spar, skin, and strut thicknesses are initialized with placeholder values. The stiffness and compliance matrix of each laminate is calculated according to classical lamination theory. From the laminate properties, the equivalent beam stiffnesses are calculated using Equations (2.6) for the spar and Equation (2.7) for the struts. The blade assembly is discretized into global stiffness matrix $[K]$ is assembled.

For the given λ and U_0 values, force coefficients C_{Fx} and C_{Fy} are identified from hydrodynamic simulation data, and dimensionalized using Equation (2.8). This load is discretized into the load vector $\{P\}$. The system $\{P\} = [K]\{u\}$ is solved for nodal displacements $\{u\}$, from which element forces can be calculated.

To size the spar, the maximum axial, shear, and moment demands in both s- and t-directions (defined in Figure 2.9) are identified. From these demands, the stress state in each ply of the spar web and flange is calculated and evaluated using the maximum stress failure criterion. If any ply is found to fail, the spar laminate thickness is increased. The increase in thickness is calculated to bring the demand-capacity ratio to just below 1 using the Secant Method. The maximum axial shear, and moment demands are used to size the strut and skin using a similar iterative process as the spar.

The new thickness of each element is used to recalculate the laminate properties and frame stiffness matrix, iterating until the design passes all stress checks. This procedure for sizing the blade assembly is performed once for each of the design load cases described in Table 2.2. If the required thickness of a component exceeds the limits of feasibility (i.e. the spar thickness exceeds the foil dimensions), then the program returns a warning.

Once the design satisfies all static stress and deflection checks, the natural frequencies of the blade are estimated using Equation (4.3). In Section 4.2.1 it is shown that the lowest frequency modes of vibration primarily involve the struts. The design algorithm increases the strut thickness if the first mode of vibration is found to be within a factor of 4.5 of the turbine rotational frequency, which would result in more than 5% dynamic amplification (shown in Figure 2.1).

Figure 2.13 diagrams the parametric design algorithm for the blades.

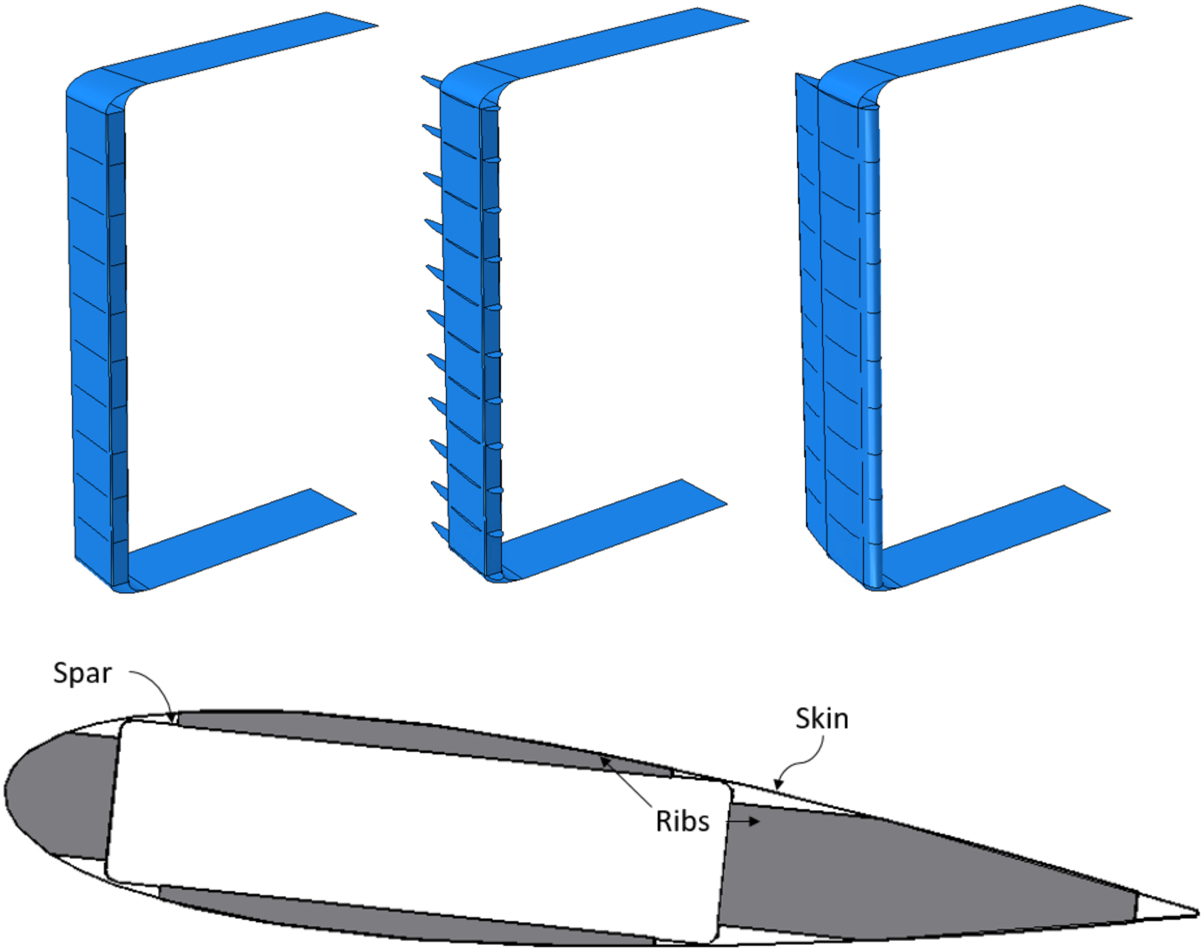

Figure 2.1: Blade assembly concept. Top left to Top right: Box-spar and supporting struts; addition of ribs; addition of skin. Bottom: Blade cross-section.

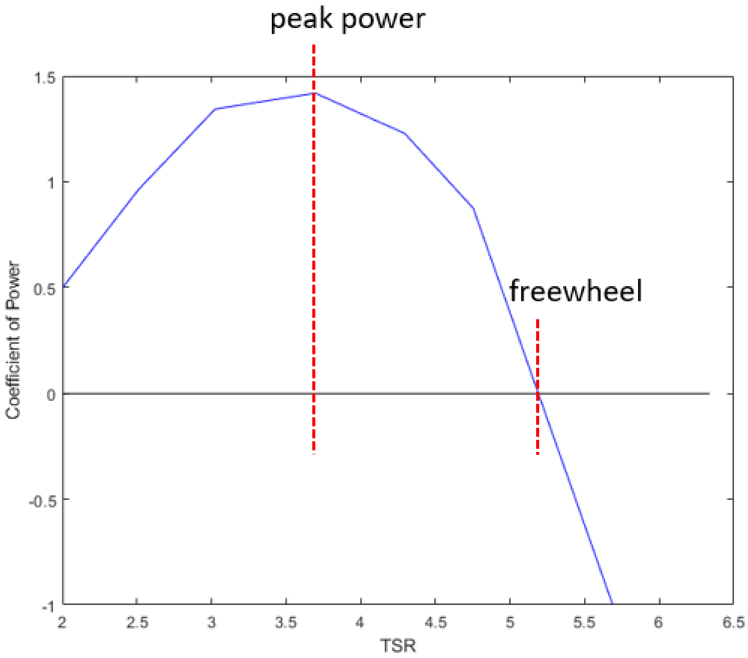

Figure 2.2: Turbine coefficient of power vs TSR. Peak power and freewheel TSRs are indicated in red.

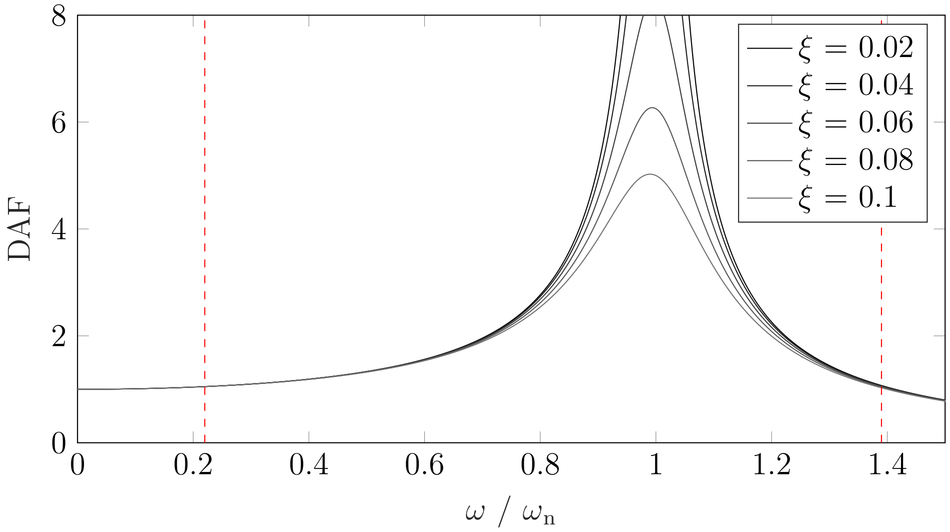

Figure 2.3: Dynamic amplification factor for several values of damping ratio ξ. Red lines indicate limits of where $R_d \leq 1.05$.

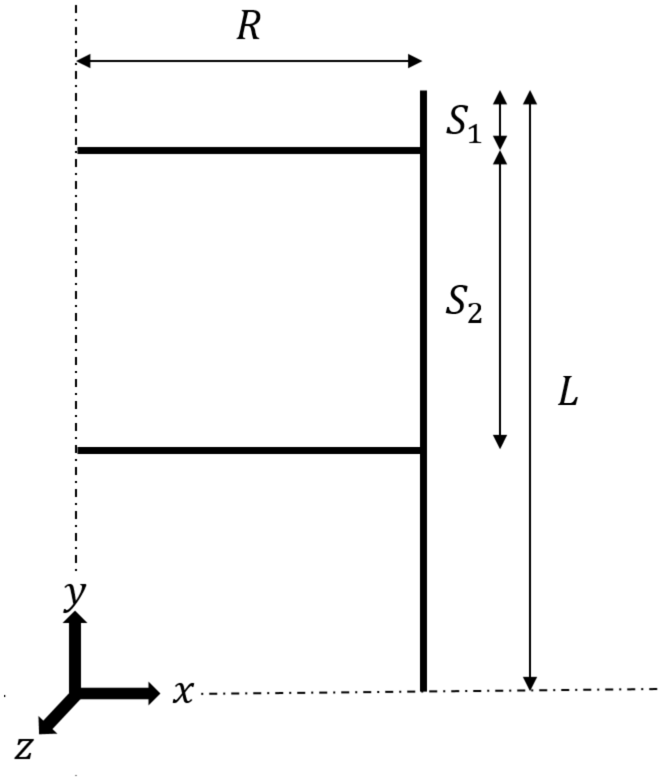

Figure 2.4: Blade frame profile with geometric parameters.

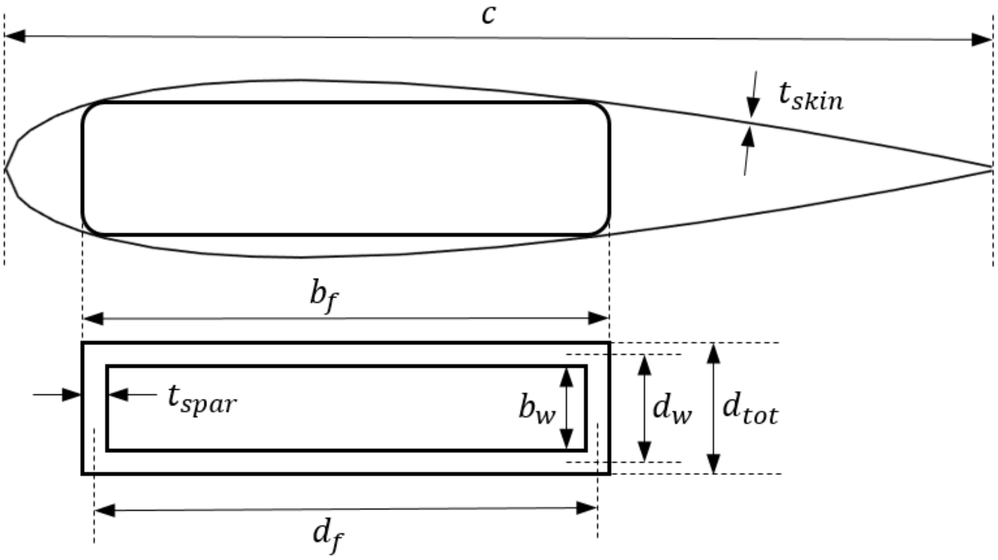

Figure 2.5: Blade profile with box-spar geometric parameters

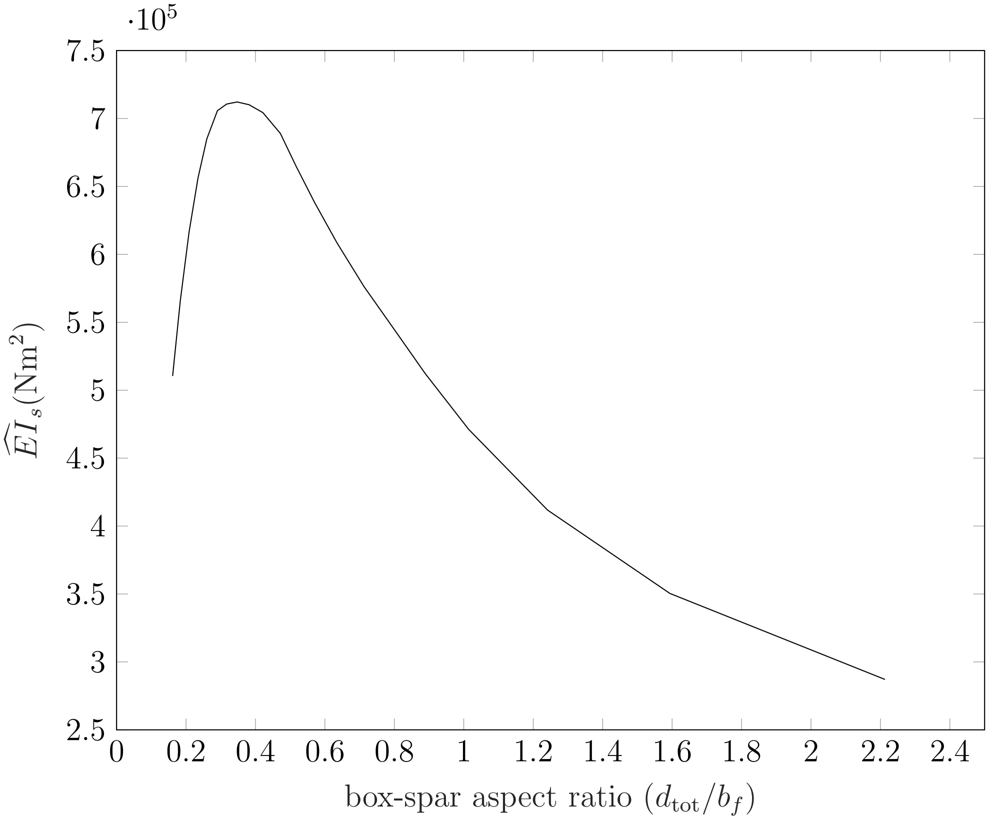

Figure 2.6: Torsional and bending stiffnesses vs. box-spar aspect ratio

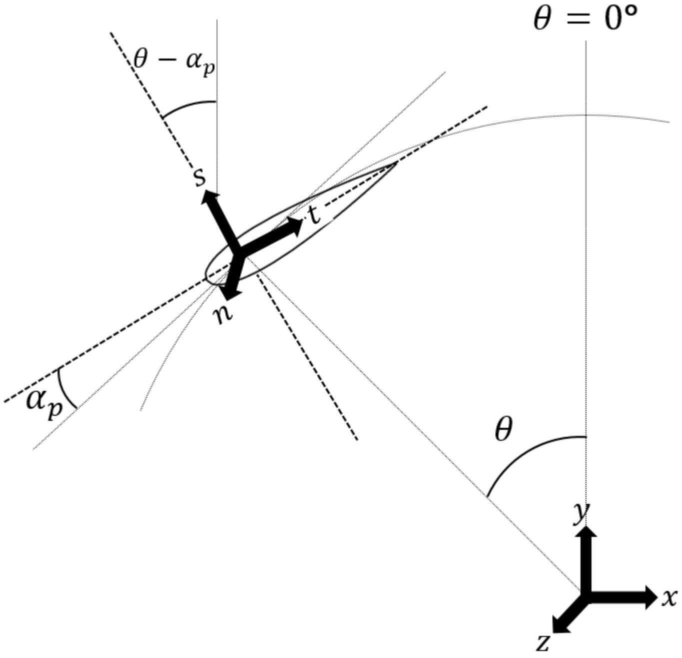

Figure 2.7: Relationship between turbine (x-y-z) and chord-referenced (n-s-t) coordinate systems for blade at azimuthal position θ

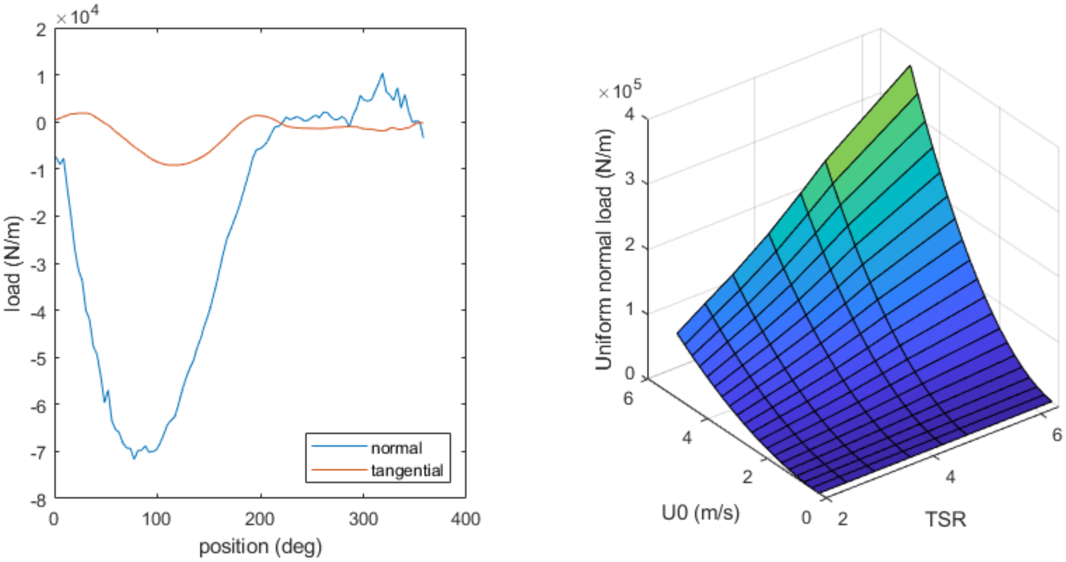

Figure 2.8: Blade load data from [7]. Left: Phase-averaged chord-referenced normal and tangential load on blade at TSR=3.7, U_0=3 m/s . Right: Maximum normal load of any phase angle for range of operational conditions.

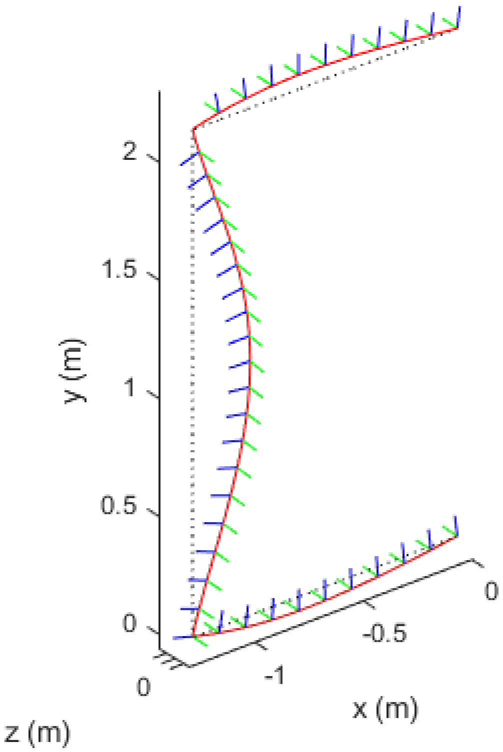

Figure 2.9: Example of blade frame model with deformations. s- and t- axes of each element are shown in blue and green, respectively.

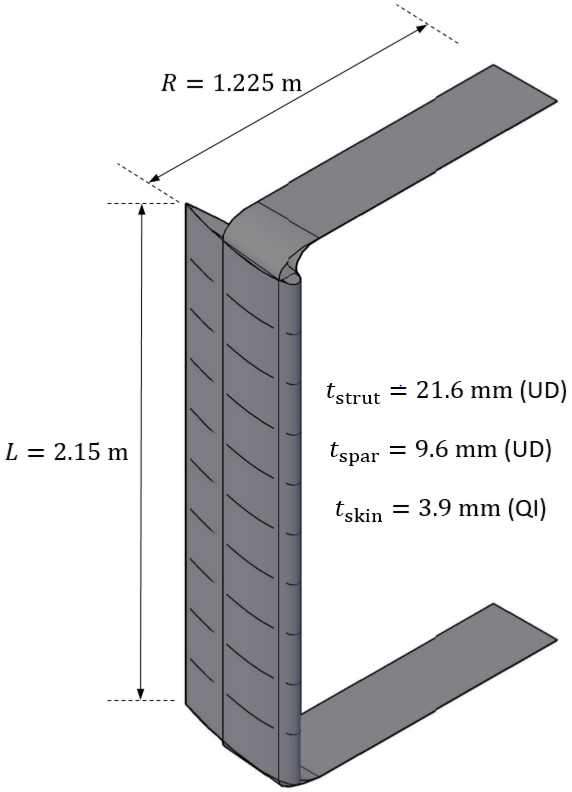

Figure 2.10: Shell finite element model geometry.

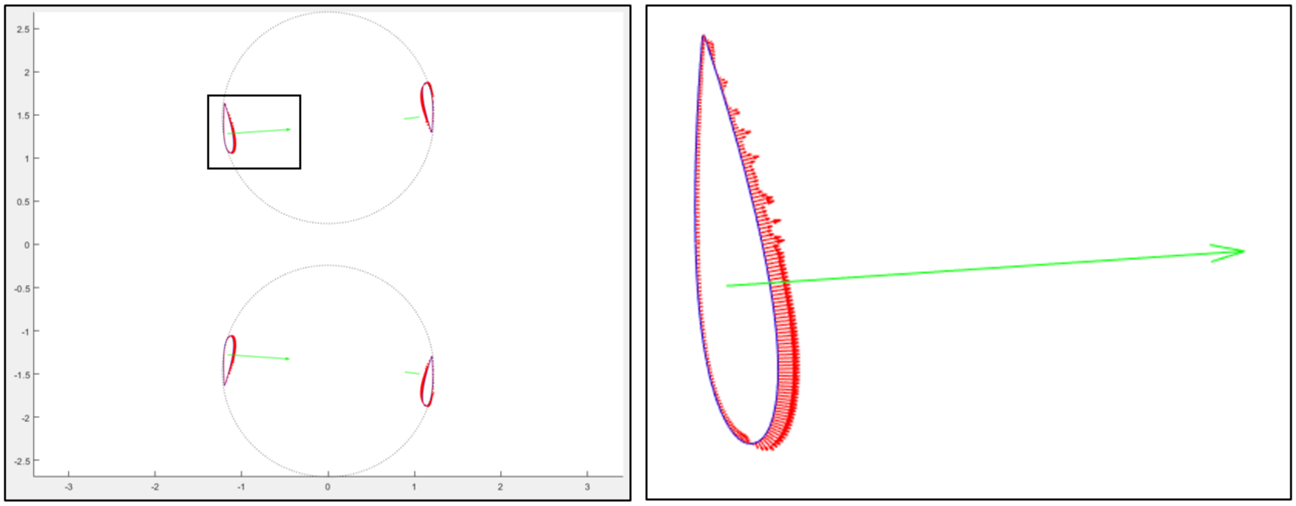

Figure 2.11: Pressure distributions and relative magnitude and direction of resultant load

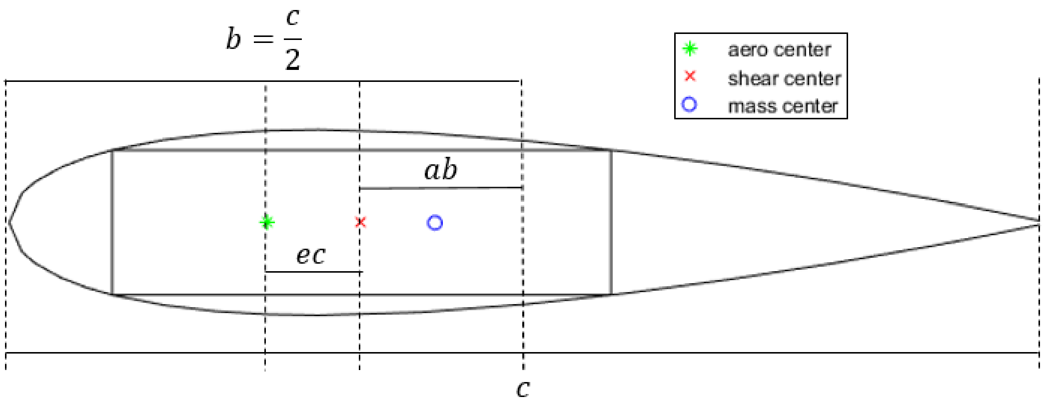

Figure 2.12: Hydrofoil shape with location of aerodynamic center, shear center, and center of mass, with geometric parameters b, ab, and ec shown

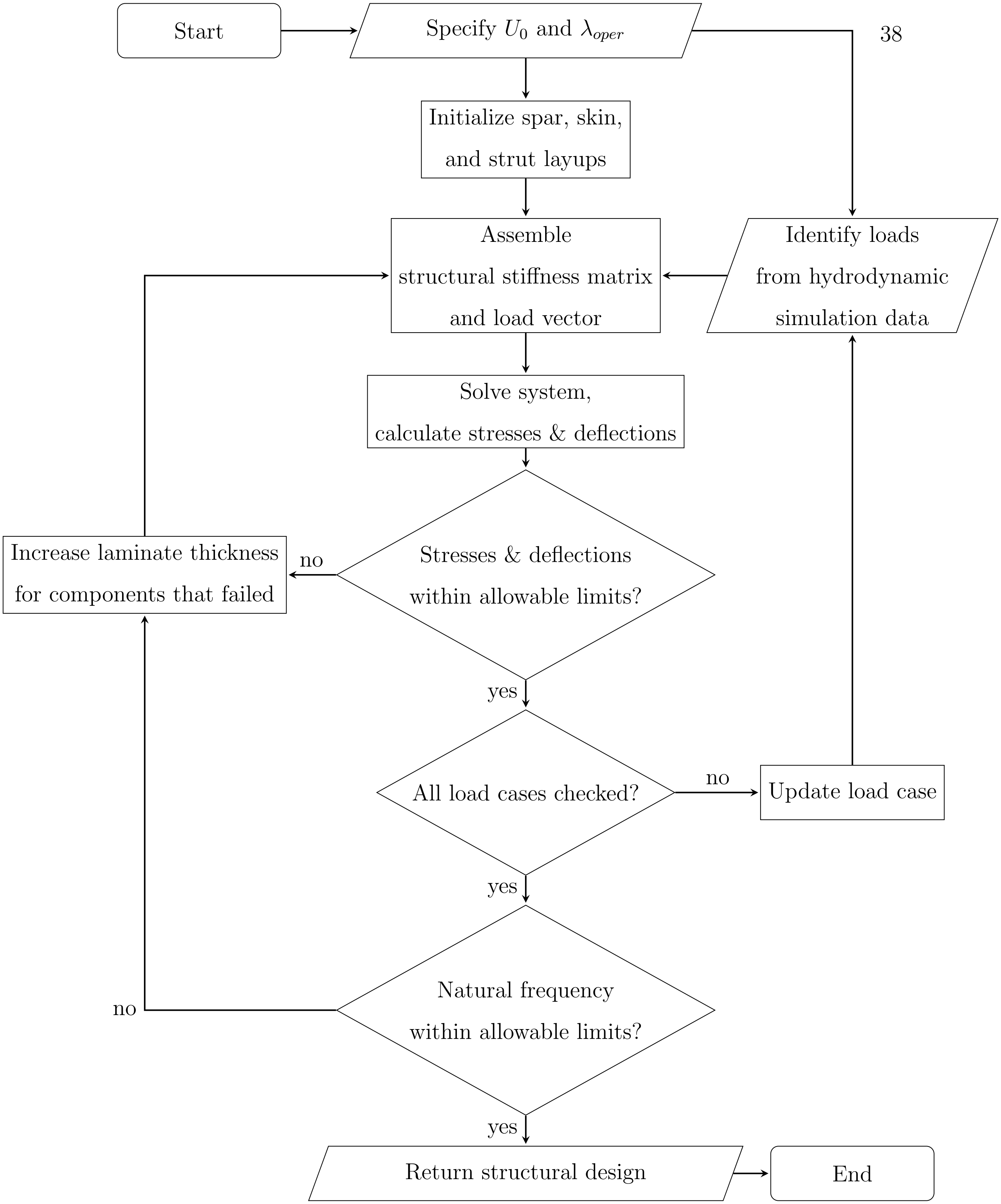

Figure 2.13: Blade parametric design algorithm

Chapter 3

SUPERSTRUCTURE DESIGN

The structural design of any turbine must consider how loads are to be transferred from the turbine into the earth. We refer to the portion of the structure between the rotor and the foundation as the "superstructure". The goal of the superstructure is to provide adequate stiffness and strength to support the turbines, while creating minimal impact on the hydrodynamic performance. In the case of vertical-axis turbine arrays, the superstructure is expected to be a more significant driver of cost than the blade structural design. The design space of possible structural layouts and materials for the superstructure is extremely large, so reasonable constraints are used to narrow it down.

3.1 Material Selection

The superstructure is designed using commercially available A36 structural steel sections. A36 steel is commonly used in structural applications for its high strength and ductility, and can be galvanized to resist corrosion in marine environments. Properties of A36 steel used in this study are listed in Table 3.1. The "endurance limit" is used to account for fatigue effects. It is defined as the stress below which the material can experience unlimited cycles without causing a fatigue failure. For steel, the endurance limit is approximately one half the yield stress.

3.2 Structural Layout

A cantilevered central shaft, as commonly seen in HAWT and VAWT, would be ideal for minimizing hydrodynamic impact, but the extreme load demands due to force amplification

Table 3.1: Properties of A36 steel used in this study.

Density	**Elastic Modulus**	**Shear Modulus**	**Yield Stress**	**Endurance Limit**
$7850\frac{kg}{m^3}$	$200 \times 10^9\text{Nm}^2$	$77.6 \times 10^9\text{Nm}^2$	$250 \times 10^6\text{MPa}$	$125 \times 10^6\text{MPa}$

from blockage effects render such a shaft infeasible. A modular 3D frame design (shown in Figure 3.1) was developed to provide a larger footprint to transfer these moment demands, while staying out of the way of the flow into the turbines. The superstructure consists of two braced frames in the streamwise direction and three portal frames in the cross-stream direction. Portal frames use moment-resisting connections to transfer horizontal loads down the structure without any diagonal bracing, and are used in the cross-stream direction in order to minimize the profile presented to the flow. In the streamwise direction, diagonal braces can be used without blocking the flow into the turbines, thus braced frames are used as they allow simpler non-moment-resisting connections. The available space for the superstructure was constrained by the modularity requirement (see Figure 1.1), as each of the three portal frames must be able to fit pre-assembled within a shipping container.

The superstructure can be anchored to the seabed using micropiles at the base of each of the six columns. Although the design of the foundation is outside the scope of this work, an estimation of the total base shear and overturning moment demands on the foundation is presented in Section 4.3.

With the frame layout determined and the allowable geometry constrained by transportability, the design of the superstructure is reduced to the problem of sizing each of the frame members. As with the blade design in Chapter 2.2, this sizing is done in a parametric framework to allow for exploration of the design space.

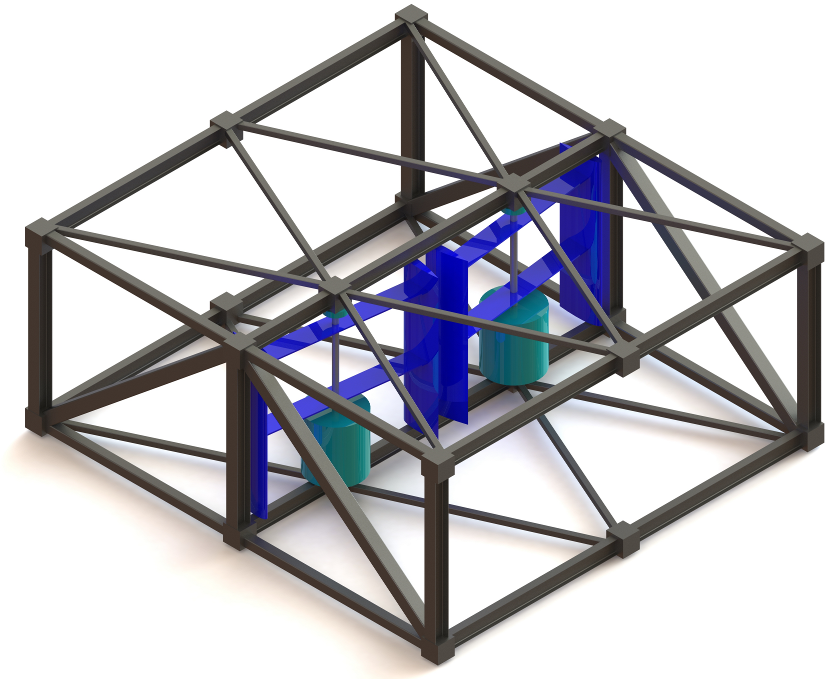

Figure 3.1: Modular superstructure concept. Rendering by Gemma Calandra.

3.3 Proposed Design Framework

As with the blades, a set of load cases and performance goals are defined for the superstructure. These load cases correspond to the normal operational conditions of the array (Service) and the likely most extreme operating condition (Ultimate).

For the ultimate load case, two extreme conditions were identified which could potentially control the structural sizing. The first extreme condition may occur if an extreme weather event causes the current speed to increase to 1.5 times the design current speed, while the turbine array remains in normal operation (similar to EOC 1 defined in [4]). The second extreme condition may occur if a loss of control braking causes one turbine in a pair to begin freewheeling (as defined in Chapter 2.3). Under normal operational conditions the counter-rotating turbine pairs will create a balanced pair of cross-stream forces, largely cancelling out the net cross-stream force generated within a cycle. However, if one turbine freewheels while the other remains in normal operation, the resulting imbalance in cross-stream forces can place significantly higher demands on the moment frames in the cross-stream direction. For design purposes, it is assumed that this failure occurs in the topmost turbine in a stack, which causes the largest moment demands in the cross-stream moment frames.

Under the two extreme conditions, the superstructue is designed to remain elastic. This is ensured by requiring the stress in each member to be below the material yield stress. However, the stress is allowed to exceed the endurance limit, because the extreme conditions are expected to occur infrequently and thus will not contribute significantly to fatigue.

Under service loads, the stress in each component must not exceed the material's endurance limit (defined in Section 3.1), and the deflection must remain within allowable limits. The allowable deflection limit is set to a 0.5% module drift ratio in order to prevent damage to bolted moment connections. This deflection limit also prevents potential collisions between the blades and the superstructure frame. The inter-story drift ratio of each module in the stack is defined as

$$\Delta = \frac{\delta_{top} - \delta_{bot}}{H}$$

where δ_{top} and δ_{bot} are the lateral displacements at the top and bottom of the module and H is the module height, as shown in Figure 3.2.

Strength reduction factors are applied to conservatively underestimate the strength of the superstructure. A strength reduction factor of $\phi = 0.9$ is applied to stress checks in bending and buckling. Load cases and performance goals are summarized in Table 3.2.

3.4 Superstructure Frame Model

All elements of the superstructure are modeled as 3D frame elements with section properties taken from the AISC shapes database. For non-symmetrical sections, the section is oriented such that the strong axis is parallel to the flow to minimize drag.

Table 3.2: Superstructure load cases and performance criteria

Load Case	**Conditions**	**Performance Criteria**
Service	Turbine operating normally at nominal U_0	• $\sigma < \sigma_e$ • $\Delta \leq 0.5\%$
Ultimate	• turbines operating normally at 1.5x nominal U_0) • one turbine shutoff at top of stack • one turbine freewheeling at top of stack	• $\sigma < \sigma_y$ • $\sigma < \sigma_b$

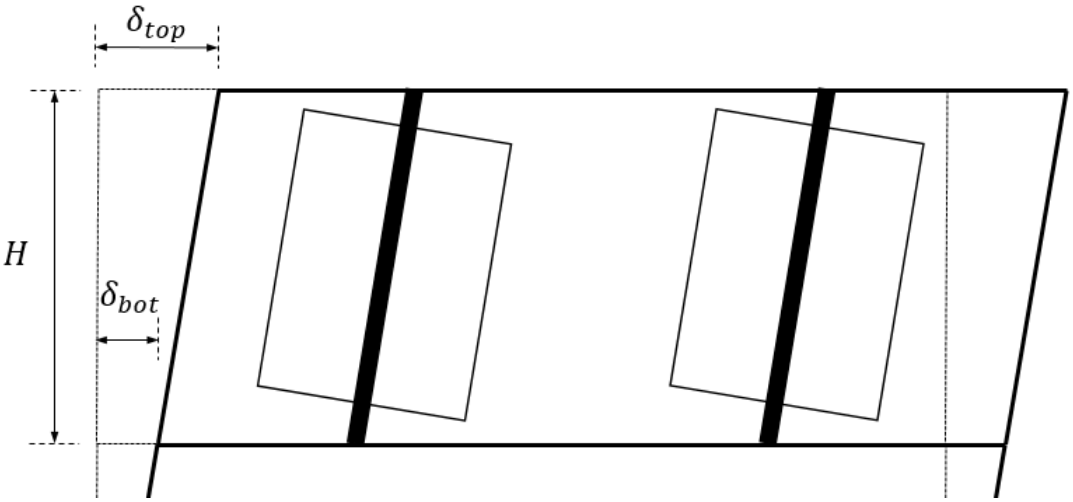

Figure 3.2: Definition of module lateral drift ratio.

Connections between elements in the cross-stream portal frames are modeled as fully fixed, while connections in the streamwise braced frames are modeled as pinned. The superstructure foundations are modeled as pinned boundary conditions at the bottom corners of each of the cross-stream moment frames.

Loading on the superstructure is derived from experiments performed by Hunt and Polagye [13], who investigated the performance of counter-rotating vertical-axis tidal turbines in confined flow at laboratory scale. Rotor forces are dimensionally scaled from the measured force on the rotor using Equation (2.8). These force coefficients include a 1.3x factor to account for turbulent fluctuations. The net streamwise force on a single turbine is shown in Figure 3.3.

Resultant forces from the blades are applied as point loads at the connection from the shaft to the frame. It is assumed that half the load is supported at the top connection and half at the bottom. Figure 3.4 depicts the superstructure frame model with applied point loads.

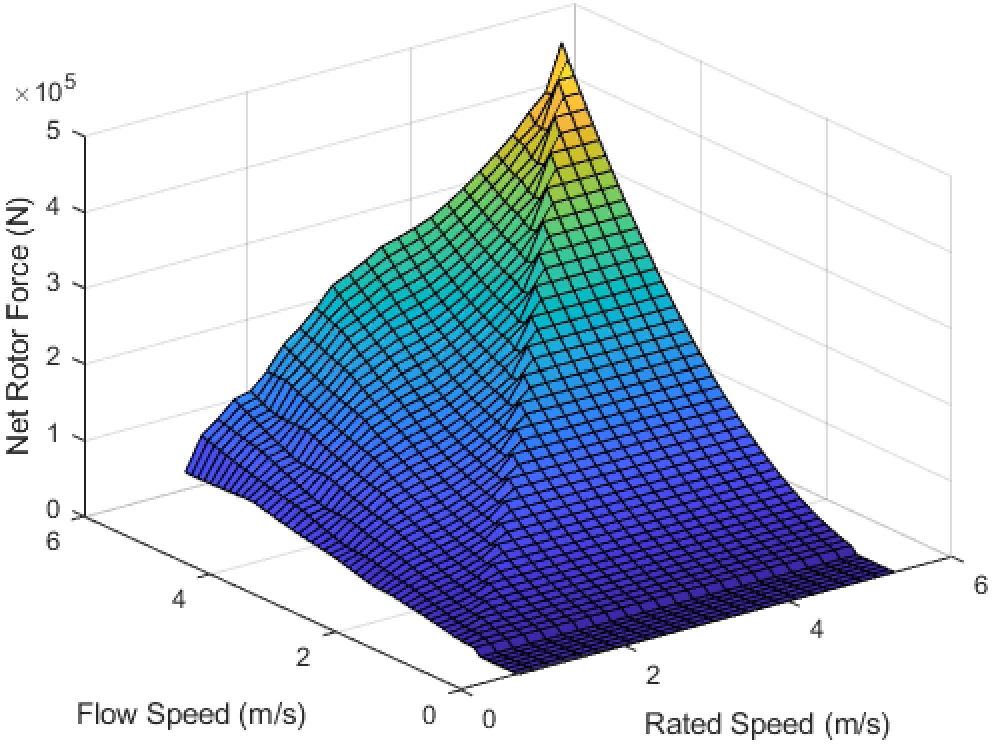

Figure 3.3: Net streamwise force applied to superstructure by single turbine in underspeed control, dimensionally scaled from experimental data from [13].

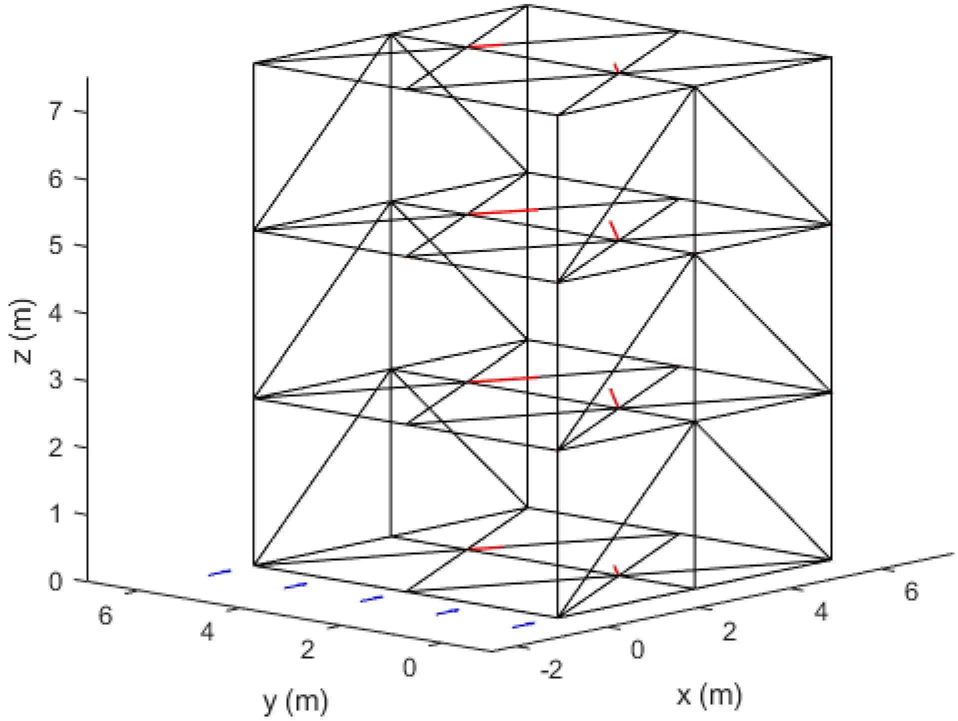

Figure 3.4: Sample superstructure frame layout for stack height = 3, rendered in MATLAB. Applied point loads shown in red, direction of current shown in blue. The apparent asymmetry in load magnitudes is due to forshortening in the rendering.

3.5 Parametric Design Algorithm

Similarly to the blade assembly, the components of the superstructure are sized using an iterative approach.

First, each member is initialized using the smallest available section from a pre-chosen library of sections. This library begins with round hollow structural sections (HSS) to minimize drag and moves up to larger wide flange (W) sections if the design requires it. The frame stiffnesses of each element can be calculated from section properties given in the AISC sections databases. These properties are used to populate the element stiffness matrices, which are then assembled into the global stiffness matrix $[K]$.

For the given inflow speed U_0 and rated speed U_R, force coefficients C_{Fx} and C_{Fy} are identified from experimental hydrodynamic data. Additionally, the self-weight and drag loads are calculated for each element. For simplicity, only the drag on the three cross-stream portal frames is considered. The drag load on these members is calculated as

$$q_{drag} = C_d * \frac{1}{2} \rho_w U_0^2 w \tag{3.1}$$

where C_d is the drag coefficient of the cross section (set equal to 1.17 for HSS sections and 2.05 for W sections) and w is the projected width normal to the flow. The turbine loads, self-weight, and drag loads are discretized and combined into the load vector $\{P\}$. Next, the system $\{P\} = [K]\{u\}$ is solved for nodal displacements, from which element forces can be calculated.

The maximum stress in each member is calculated using Equation X:

$$\sigma_{max} = \frac{P}{A} + \frac{M}{S} \tag{3.2}$$

where P is the axial load, A is the cross-sectional area, M is the maximum bending moment, and S is the cross-sectional section modulus.

From this stress, the Demand/Capacity Ratio (DCR) is calculated as the ratio of σ_{max} to $\phi_b \sigma_{allow}$, where σ_{allow} is set equal to the yield stress for the ultimate load cases or to the endurance limit for the service load case, and $\phi_b = 0.9$ is the strength reduction factor for bending, found in the AISC Steel Construction Manual [1].

Buckling is checked for each member by comparing its axial load to the Euler critical buckling load

$$P_{cr} = \frac{\pi^2 E I_{tt}}{(KL)^2} \tag{3.3}$$

where E is the material elastic modulus, I_{tt} is the cross-sectional weak-axis moment of inertia, L is the unbraced length, and K is the effective length factor. The DCR for buckling is calculated for each member as the ratio of the axial load P to the factored critical load $\phi_b P_{cr}$.

Any member with $DCR > 1$ is increased to the next structural section in the library. For efficiency and simplicity of design, each class of member is increased together, e.g., if one vertical brace fails than all vertical braces will be increased. If any module is found to exceed the limit of $\Delta \leq .005$ in either direction, then the elements controlling lateral displacment in that direction are increased.

The above limits are checked for each of the design load cases defined in Table 3.2. If any design checks are failed, the model is re-run with updated member sizes. This iterative process is continued until all design checks are passed. The result of this is a design which satisfies all requirements and heuristically minimizes weight. This design is not guaranteed to be globally optimal in terms of weight, but in practice gives a design which is sufficient for estimation of structural costs.

A flowchart describing the parametric design algorithm for the superstructure is shown in Figure 3.5.

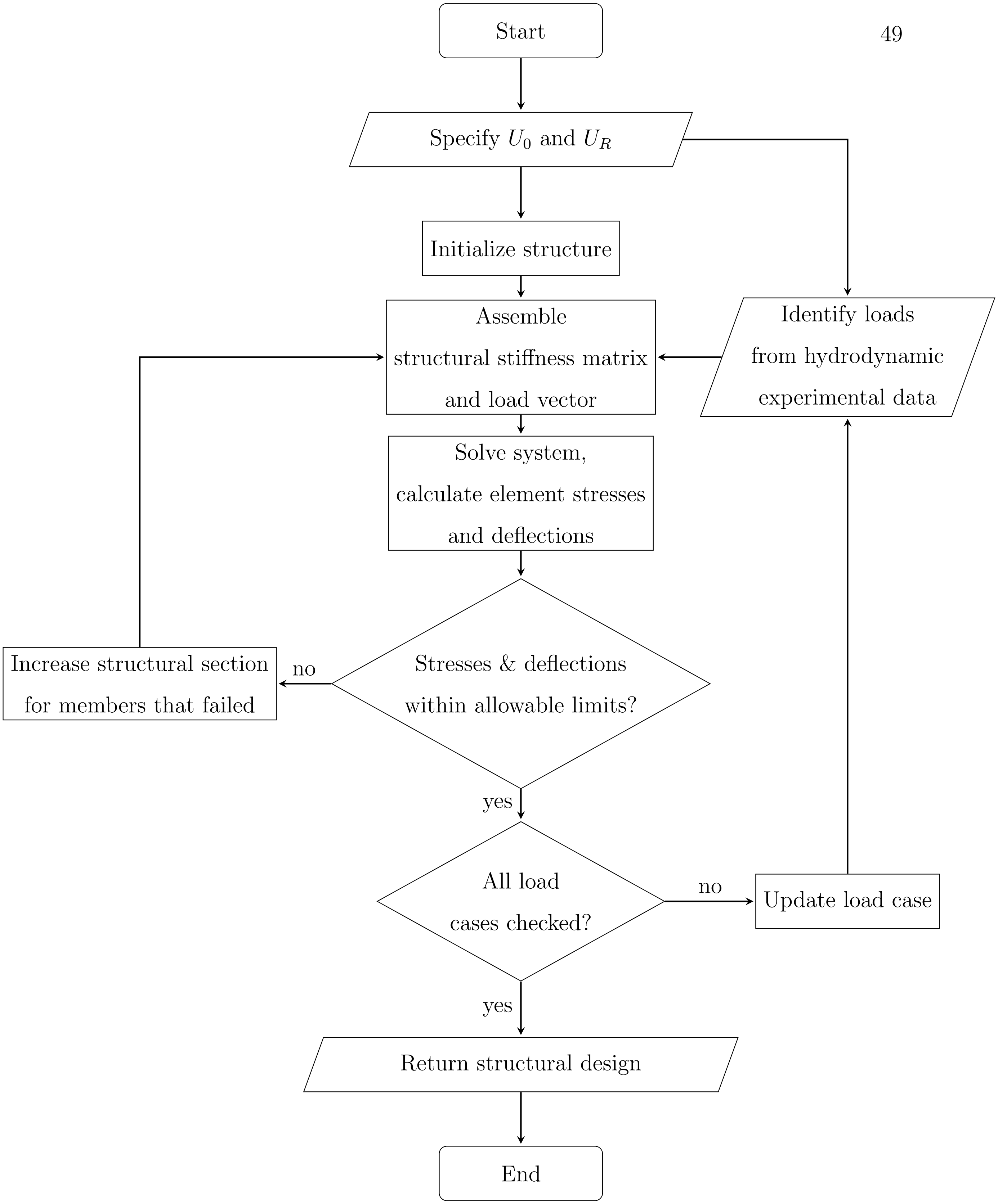

Figure 3.5: Superstructure parametric design algorithm

Chapter 4

RESULTS

4.1 Comparison of Blade Models

In this section, stresses and deflections of the blade are analyzed for a single design (detailed in Section 2.5) using the shell FEM. These results are compared to the values predicted by the simplified frame model.

Some postprocessing of the FEM stresses is performed prior to visualization. Because the shell FEM does not properly model the interface between the ribs and spar, there are some stress concentrations in the transverse direction at the rib connections. In reality, the ribs (or foam infill) would not be so rigidly connected to the spar, and these stress concentrations would not be present. To properly visualize the maximum stress criterion without being drowned out by these spurious stress concentrations, the transverse failure strengths S_2^+ and S_2^- are artificially set to a high value of 10^9 GPa. From there, the maximum stress criterion (Equation (2.14)) is used to visualize the stresses in the blade assembly.

Figure 4.1 shows the maximum stress criterion with the exclusion of transverse stresses. Stresses remain within allowable limits, with the exception of stress concentrations at the span ends and in the connection between the spar and strut. These stress concentrations are likely a consequence of the (lack of) connection details, and could be mitigated through proper connection design. While designing for such stress concentrations is important, it is unlikely to significantly alter the total material cost of the design, which is the primary focus of this study.

The stress distribution also differs from the simplified model in its general shape. The frame model designed the spar assuming a linear stress distribution based on Euler-Bernoulli beam theory, which would predict a uniform stress in the flange. The shell model shows that

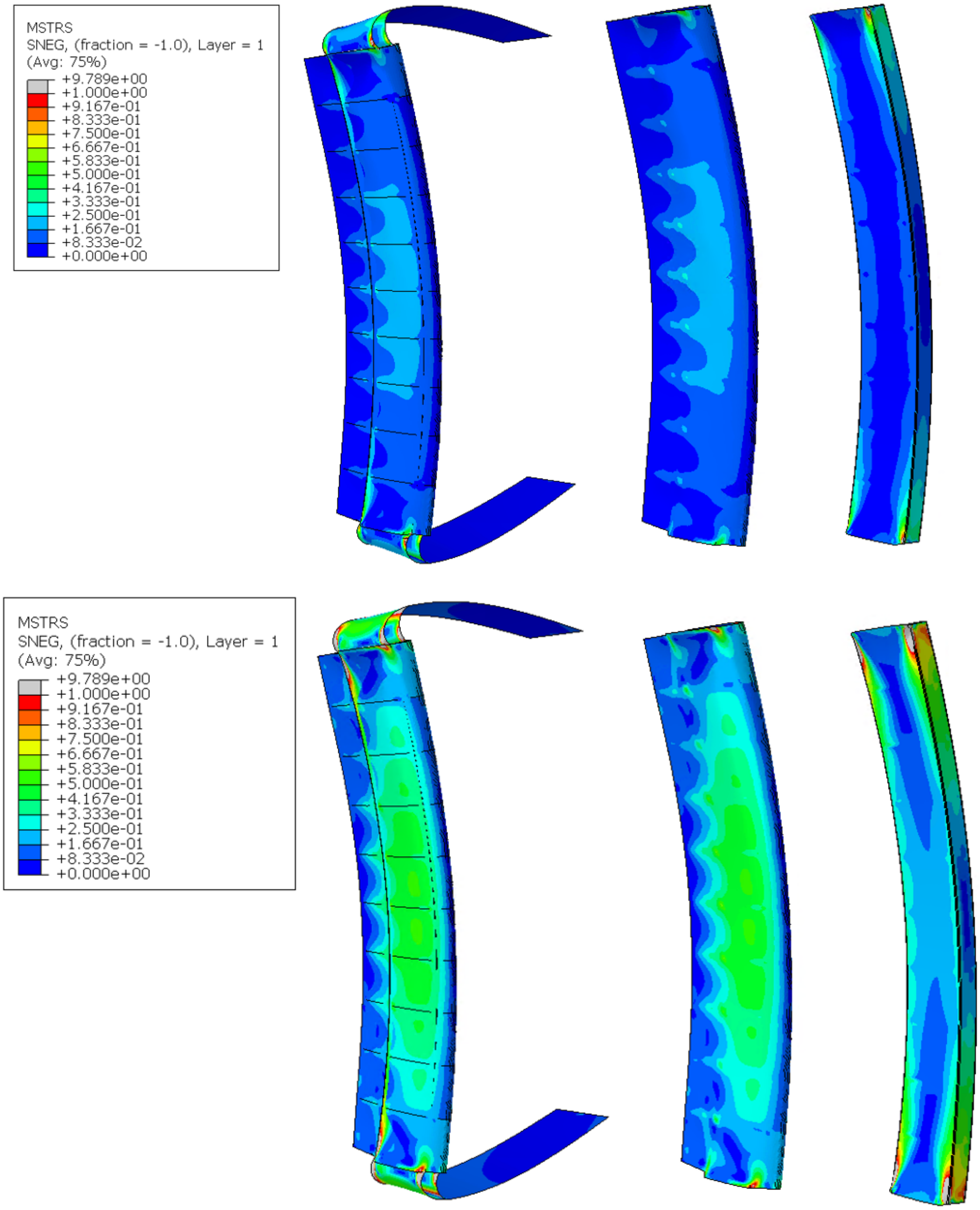

Figure 4.1: Maximum stress criterion in full blade assembly, skin, and spar at operational (top) and extreme (bottom) loading. A value ≥ 1 indicates that one or more stress components exceed the material strength. Transverse stresses are ignored to avoid spurious stress concentrations at rib connections.

the actual stress distribution in the flange is more concentrated near the webs. This is due to the phenomenon of shear lag, in which the flanges are not sufficiently connected to one another to satisfy the assumption that plane sections will remain plane in the deformed shape. Figure 4.2 shows that magnitude of the maximum normal stress in the spar aligns roughly with the stress predicted for a beam fixed at both ends. However, shear lag causes higher stresses at the corners and lower stresses in the center of the flange.

The stress distribution in the skin also differs from the distribution assumed in its design. Rather than being controlled by local bending in the spans between ribs, the maximum stress in the skin appears to come from the bending action of the blade. However, the skin still shows stresses within allowable limits.

The displacements in the shell FEM can be compared to those predicted by the simplified model. Figure 4.3 shows the net normal and twist displacements of the centerline of the box-spar. Euler-Bernoulli beam theory can be used to back-calculate the equivalent stiffness of the blade based on the maximum displacment, assuming a uniformly loaded simply supported beam:

$$\widehat{EI}_s = \frac{5wL^4}{384\delta_{\max}} = 9.26 \times 10^5 \mathrm{Nm}^2 \tag{4.1}$$

Similarly, Saint-Venant torsion theory can be used to calculate the equivalent torsional stiffness assuming a uniformly loaded beam with ends fixed against torsion:

$$\widehat{GJ} = \frac{TL^2}{8\phi_{\max}} = 7.86 \times 10^5 \mathrm{Nm}^2 \tag{4.2}$$

Figure 4.3 shows the normal and twist displacements from the FEM compared to the theoretical shape assuming the stiffnesses given by Equations (4.1) and (4.2). The FEM and theoretical curves give good agreement, indicating that the beam is behaving as a simply supported beam. However, the bending stiffness $\widehat{EI}_s$ calculated from the FEM is 30% lower than the stiffness predicted by the frame model (including the skin moment of inertia in the frame model stiffness), likely due to the effects of shear lag.

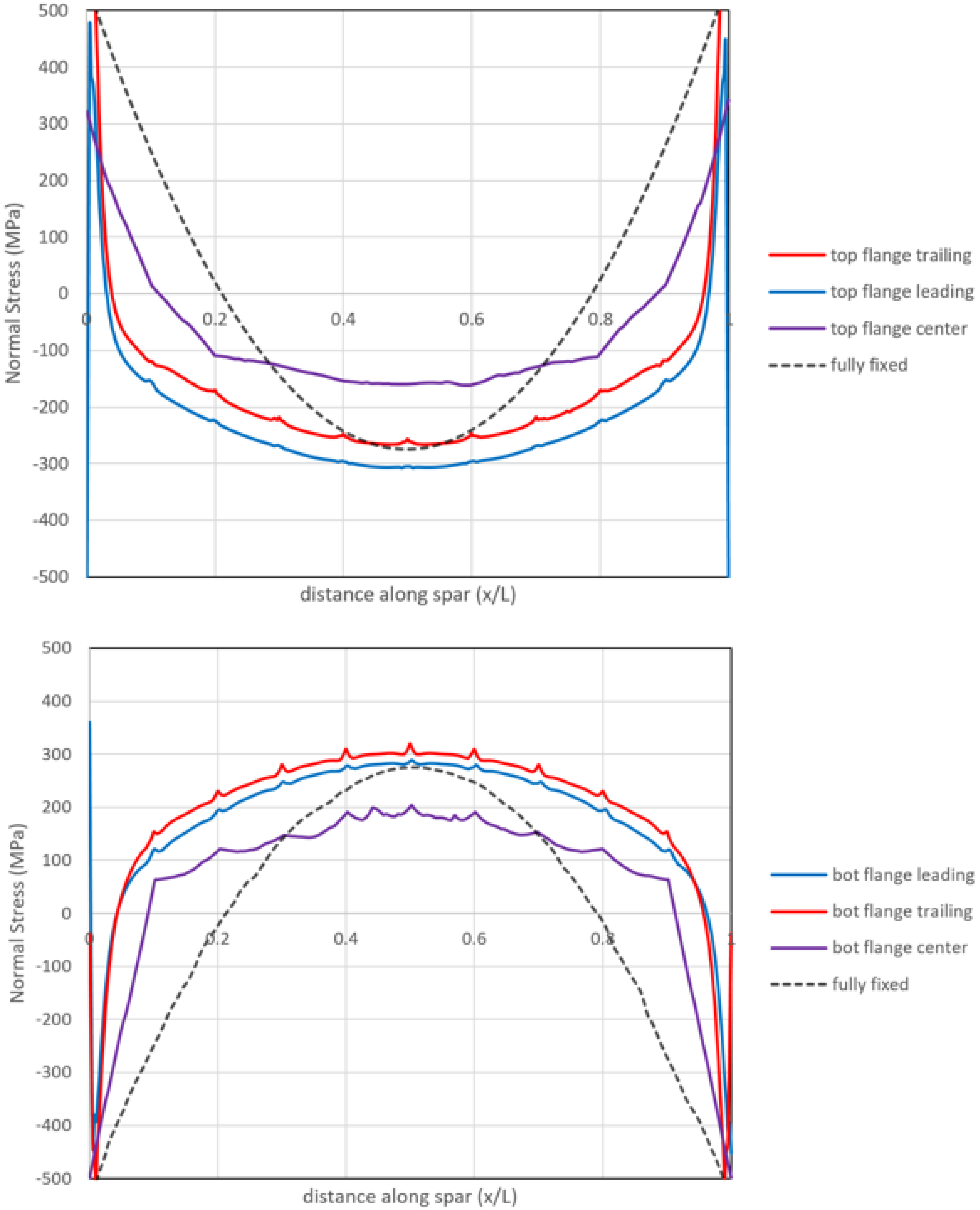

Figure 4.2: Normal stress (σ_1) plotted along length of spar in top flange (top) and bottom flange (bottom) at the leading corner, trailing corner, and center of the flange. Stress at the corners is higher than at the center due to shear lag. Small stress concentrations can be seen at the rib locations. Dashed lines indicate the stress predicted by Euler-Bernoulli beam theory for a beam fixed at both ends with a uniformly distributed load.

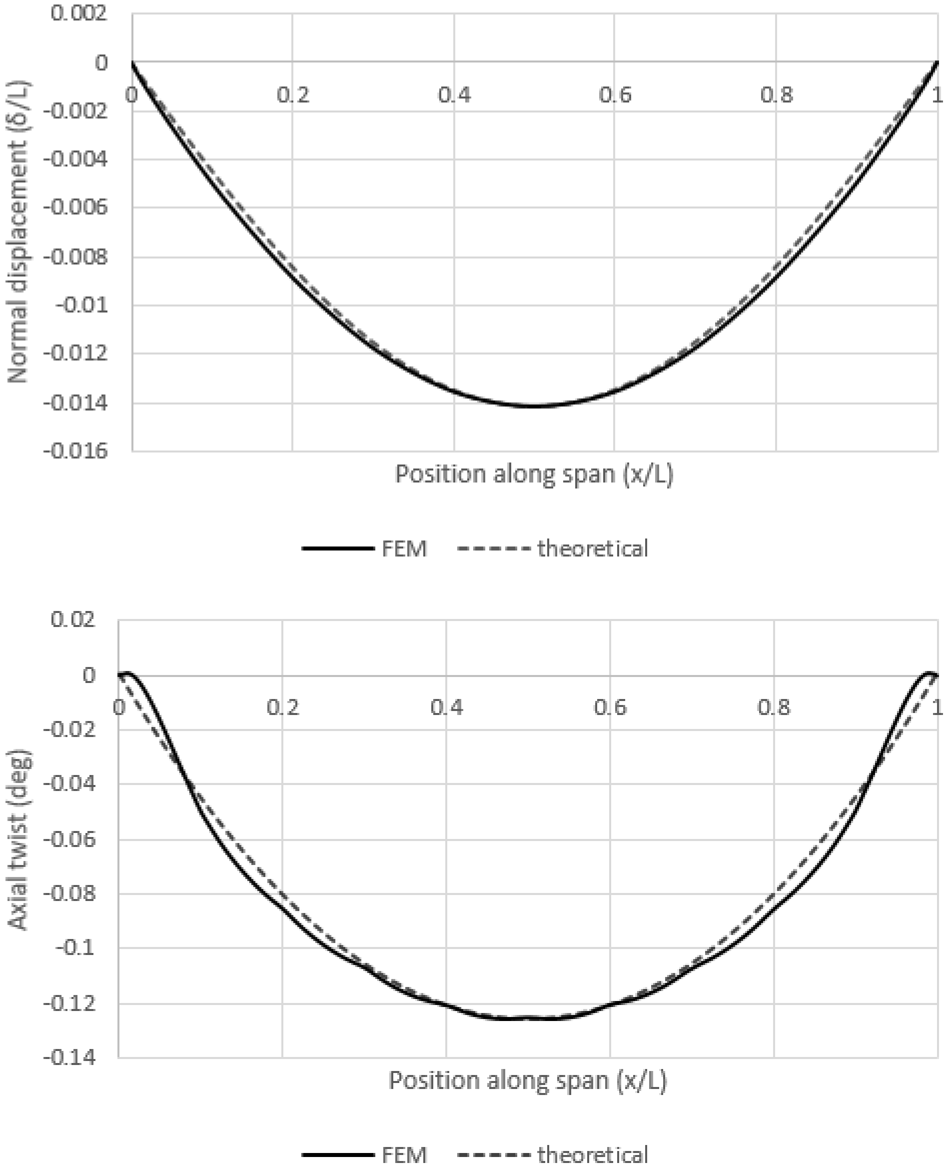

Figure 4.3: Net centerline normal (top) and twist (bottom) displacements under service load conditions. Dashed lines indicate theoretical shape of curve with the same maximum displacement according to Euler-Bernoulli beam theory and Saint-Venant torsion theory.

The shell FEM shows that stresses and deflections are higher than those predicted by the simplified blade model. However, the agreement is close enough for purposes of cost estimation and design space exploration. Once a design has been settled upon, the more precise FEM can be used to analyze stresses and deflections.

4.2 Results of Parametric Blade Design

The blade parametric design algorithm outlined in Section 2.7 was performed on a set of input parameters representative of the expected operating conditions of the blade, shown in Table 4.1. Figure 4.4 shows the required spar wall thickness, skin thickness, and strut thickness resepctively at each input combination of current speed and TSR. Figure 4.5 shows the controlling limit state and load case for the spar design.

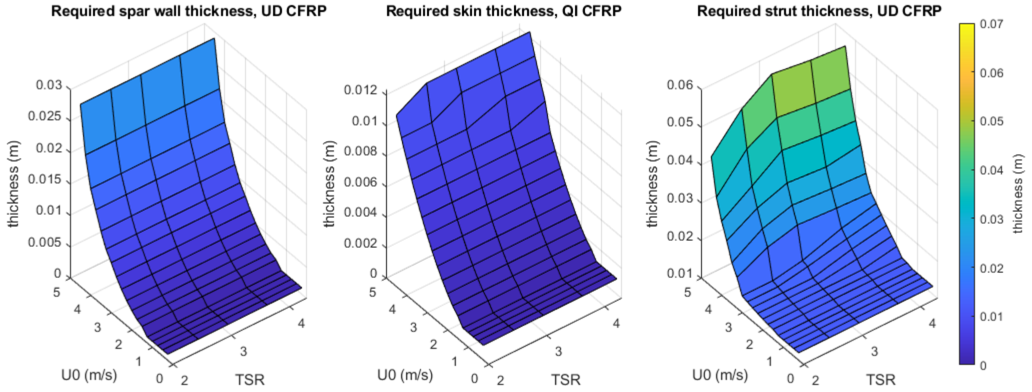

Figure 4.4: Required spar, skin, and strut thicknesses for range of input current speeds and tip speed ratios. Points above $U_0 = 4.5$ m/s are missing, indicating that the required spar thickness exceeds the limits of feasibility.

Figure 4.5 shows that the design of the blade is largely controlled by stress at the ultimate load case. In the regions where the ultimate load case controls, the design spar thickness is independent of the operational TSR, because the most extreme loads occur in the freewheel condition. At high freeflow speed and operational TSR, the pitch deflection limit state necessitates a larger skin thickness. The strut is the only component for which the sizing is

Table 4.1: Parameters and design variables for superstructure parametric design study

Geometric Parameters	**Symbol**	**Value**
Blade length	L	2.15 m
Turbine radius	R	1.225 m
Chord/Radius	c/R	0.47
Preset pitch	α_p	6°
Design Parameters	**Symbol**	**Value**
Service Deflection Limit	$\delta_{\max}$	.03L
Service Pitch Limit	$\Delta\alpha_{\max}$	1°
Freeflow speed factor	γ_{U_0}	1.3
Strength Reduction Factor	ϕ	0.75
Input Variables	**Symbol**	**Range**
Freeflow speed	U_0	0-5 m/s
Tip speed ratio	λ, TSR	0-6.33

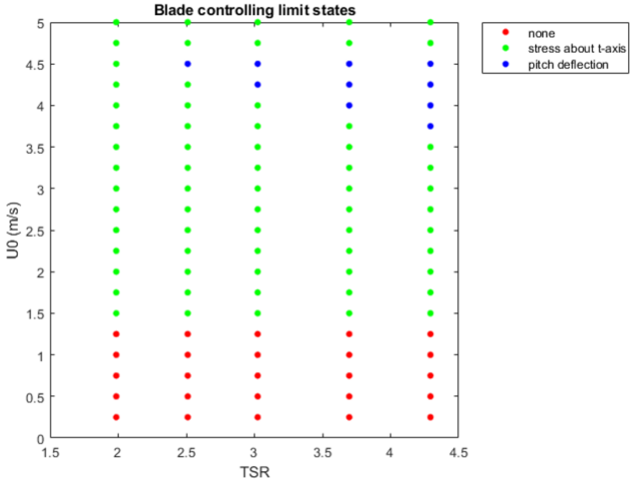

Figure 4.5: Spar controlling limit states and load cases. 'None' indicates that the initial thickness value of .001m was sufficient for the loads. Stress controls at the Ultimate load case while deflection controls at the Service load case for all points shown.

significantly affected by operational TSR, because the strut thickness tends to be controlled by resonant frequency requirements.

It should be noted that the design of the blade may still be controlled by deflection at service load if it is found that the allowable deflection limits must be set very strictly to avoid negative hydrodynamic impacts. For example, Figure 4.6 shows how the designs change if the allowable normal deflection is reduced from .03L to .01L. This stricter deflection limit causes the design to be controlled by deflection at service load for higher operational TSRs.

Figures 4.4-4.6 demonstrate the feasibility of the box-spar design concept for nominal current speeds ranging from 0-4.5 m/s and operational TSR ranging from 0-4.3. For current speeds exceeding 4.5 m/s, designing for stress at extreme load case causes the required spar wall thickness to exceed the space within the foil. For operational TSRs exceeding 4.3, the design may be infeasible at high current speeds due to high deformations, although this depends on the deformation limits chosen. It should be noted that these are not hard limits on the design of turbine arrays; they are dependent on the input parameters. For example,

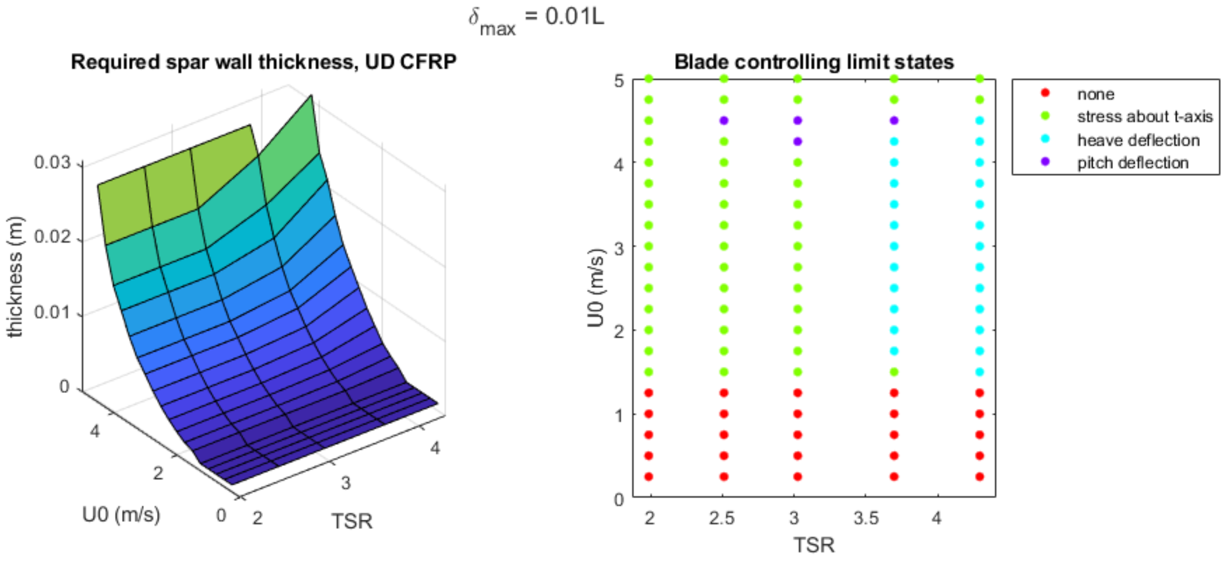

Figure 4.6: Required spar thickness and controlling limit states with deflection limit reduced to .01L. Chord-normal blade displacement (here denoted "heave deflection") controls at a lower operational TSR compared to Figure 4.4, and the limits of feasibility are further reduced.

a more efficient placement of struts would reduce the bending moment demands and permit higher load conditions.

A full integrated economic analysis of the turbine arrays has not yet been conducted. It may be found that the inclusion of the freewheel condition in the ultimate load case results in excessively costly blades, or removes too much of the design space to be acceptable. In that case, other strategies may be adopted to reduce the load on the blades, such as control and/or braking strategies which mitigate the risk of a turbine going into the freewheel state.

4.2.1 Dynamic Characteristics

Dynamic characteristics of a sample design are calculated as described in Section 2.6 to identify any potential for resonance. The first three "in-air" (not considering any fluid effects) natural frequencies and mode shapes of a typical design are shown in Figure 4.7. Table 4.2 compares the first three natural frequencies in air, in still water (setting $U_0 = 0$), and in water with $U_0 = 3$ m/s. The blade design used in these calculations is the output of the parametric design algorithm for $U_0 = 3$ m/s, $\lambda_{\text{oper}} = 3.69$, and other parameters specified in Table 4.1.

Table 4.2: Example of fluid effects on blade natural frequencies.

Mode	**In-air frequency**	**In still water**	**In water @ $U_0 = 3$ m/s**
1	6.28 Hz	3.90 Hz	3.90 Hz
2	69.09 Hz	18.47 Hz	17.37 Hz
3	88.95 Hz	29.81 Hz	29.66 Hz

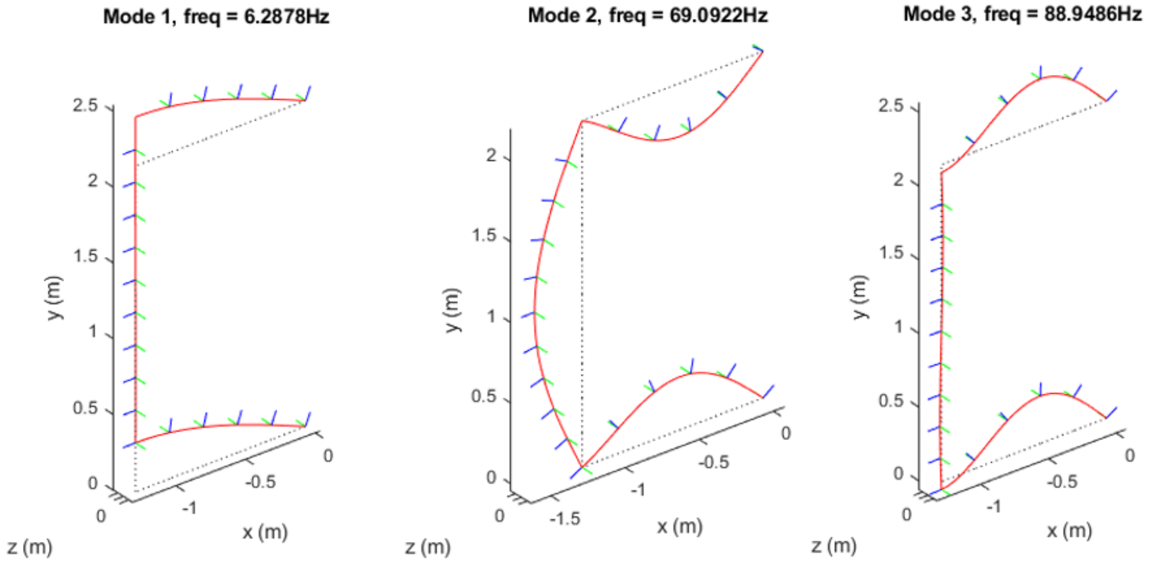

Figure 4.7: First 3 in-air mode shapes and corresponding natural frequencies.

Table 4.2 shows that the presence of the water has a significant effect on the natural frequencies, but the flow speed only has significant effects on some frequencies. The in-air natural frequencies can be compared to closed-form approximations to confirm that they are close to the expected behavior. The first mode resembles two cantilevered beams with a mass on the end. The natural frequency of such a system is

$$f_c = \frac{1}{2\pi}\sqrt{\frac{2 * 3\widehat{EI}_s/R^3}{m_{\text{blade}}}} = 10.37Hz \tag{4.3}$$

where f_c is the frequency in Hz, $\widehat{EI}_s$ is the in-plane bending stiffness of the strut, R is the turbine radius, and m_{blade} is the total mass of the blade. This roughly agrees with Table 4.2, with the 15% difference due to the mass of the struts being unaccounted for in the closed-form approximation. For efficiency, the approximation given in 4.3 is used in the parametric design algorithm.

Likewise, the second mode resembles a beam in free vibration supported at both ends by rotational springs. The frequency should be in between that of a simply supported beam (f_{ss}) and a fully fixed beam (f_{ff}), which have natural frequencies

$$f_{\text{ss}} = \frac{\pi}{2}\sqrt{\frac{\widehat{EI}_s}{qL^4}} = 73.32Hz$$

,

$$f_{\text{ff}} = 3.56\sqrt{\frac{\widehat{EI}_s}{qL^4}} = 166.18Hz$$

where $q = m_{\text{blade}}/L$ is the blade mass per unit length. The blade assembly having a computed frequency of 69.09 Hz suggests that the blade's behavior is much closer to simply supported than fully fixed.

The relationship between the resonant frequency of the blade and the rotational speed of the turbine is shown in Figure 4.8 . As the turbine's rotational rate increases, the speed of the blades relative to the water (U_n) increases, which reduces the equivalent stiffness of the blade via Equation 2.17, resulting in a lower natural frequency of the blade assembly. Resonance would occur where the red line intersects the line of blade natural frequencies, however this does not occur until a TSR of approximately 10, which is well above even the predicted freewheel TSR of the turbine.

It can be seen in Figure 4.8 that mode 2 (the middle series of frequencies) is most affected by increases in TSR, while modes 1 and 3 are relatively unaffected. At a TSR of approximately 13.5, the frequency of mode 2 becomes lower than that of mode 1, although this too is far outside the expected range of conditions which the turbine will actually experience. Thus, the most critical frequency for design is the in-plane swaying mode, which is controlled by the stiffness of the supporting struts. For this reason, the parametric design code controls the natural frequency by modifying the stiffness of the struts.

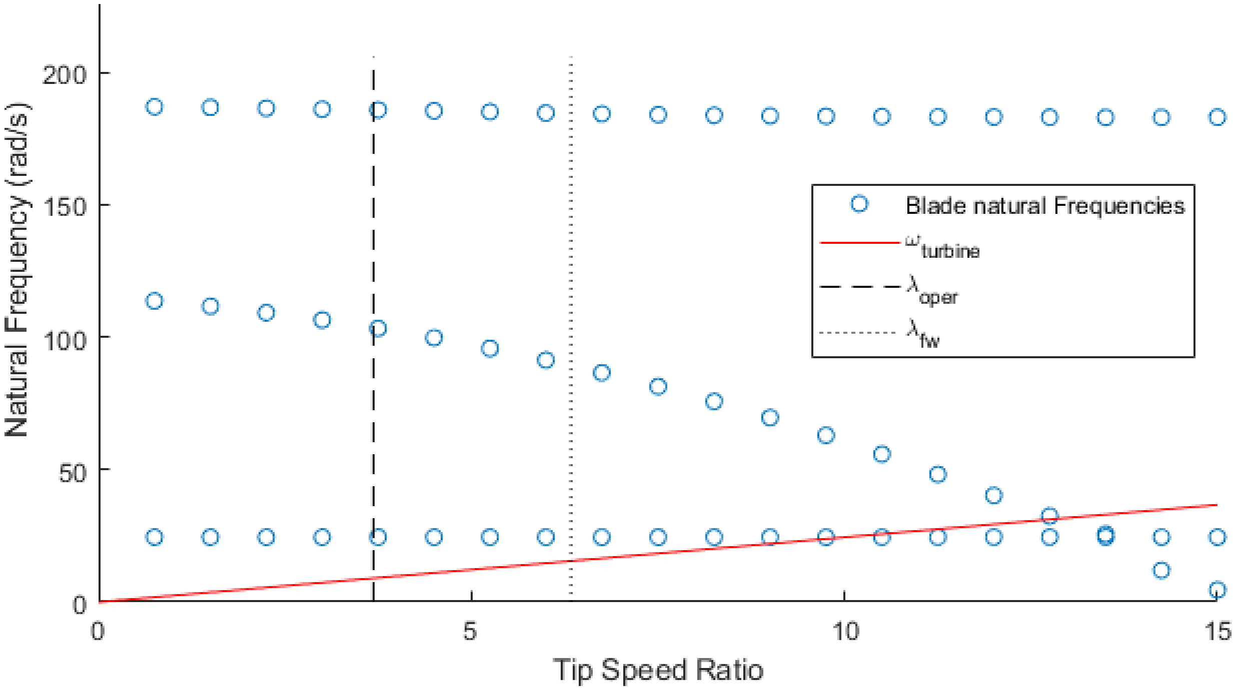

Figure 4.8: Scatter of first 3 blade natural frequencies vs. TSR at a constant freeflow speed of $U_0 = 3$ m/s. Blue dots indicate the first 3 natural frequencies of the blade at a given TSR. The red line indicates the natural frequency corresponding to the rotational frequency of the turbine.

4.2.2 Instabilities

Equations (2.18) and (2.19) are used to predict the rotational rates at which the torsional divergence and centrifugal buckling instabilities occur for the above sample blade design. At a freeflow speed of 3 m/s, centrifugal buckling is predicted to occur at at a frequency of $\omega = 1,036$ rad/s, corresponding to a TSR of $\lambda = 423$, extremely far from the operational range of the turbine. Torsional divergence is predicted to occur at a net flow speed relative to the blade of $U_n = 119$ m/s, which would occur if the turbine were to freewheel at a freeflow speed of $U_0 = 16.3$ m/s, which is again far from realistic conditions. These results suggest that these instabilities are unlikely to control the structural design of the blades.

4.3 Results of Parametric Superstructure Design

The superstructure parametric design algorithm outlined in Section 3.5 was performed on a set of input parameters representative of the expected operating conditions of the turbine array, shown in Table 4.3. Figure 4.9 shows the total mass of structural steel required at each input combination of current speed, turbine rated speed, and array stack height. Figure 4.10 shows the total base shear and overturning moment demands for a stack height of 6, which can be used to estimate foundation requirements and costs.

Feasible superstructure designs can be found for all sampled points ranging from 0-5 m/s freeflow speed and 0-5 m/s rated speed. The required mass of the superstructure roughly follows the shape of the maximum streamwise load curve shown in Figure 3.3. The discrete steps in the mass plot occur when a set of members is updated to the next largest available structural section. Stack height has a significant impact on the required mass, as the loads accumulated from the upper modules must be transferred into the foundation by the lower modules.

Figure 4.11 shows the controlling limit state for the superstructure design at each input combination of current speed and turbine rated speed. By nature of the design algorithm, it is tricky to identify a single limit state which controls the design. Different members

Table 4.3: Parameters and design variables for superstructure parametric design study

Geometric Parameters	**Symbol**	**Value**
Module height	H	2.5 m
Module cross-stream width	W	6 m
Module streamwise depth	D	6 m
Turbine control strategy	$\sim$	underspeed
Design Parameters	**Symbol**	**Value**
Freeflow speed factor	γ_{U_0}	1.5
Strength reduction factor	ϕ	0.9
Drift limit	$\Delta_{\max}$	.005
Input Variables	**Symbol**	**Value**
Array stack height	N	$1-6$
Freeflow speed	U_0	0-5 m/s
Turbine rated speed	U_R	0-5 m/s

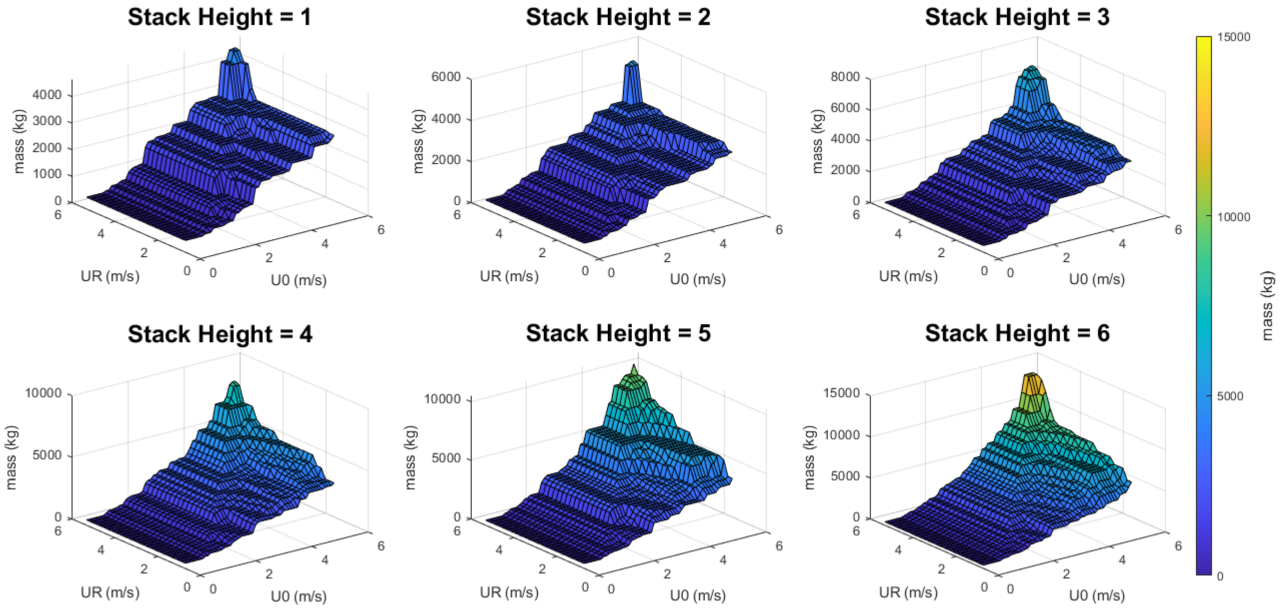

Figure 4.9: Required mass of structural steel per module for each combination of rated speed (U_R), inflow speed (U_0), and stack height.

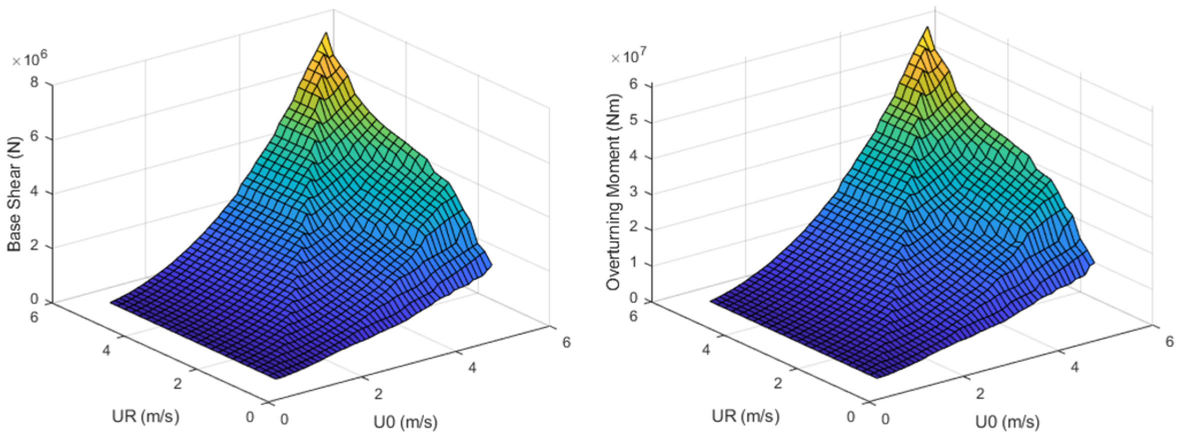

Figure 4.10: Sample output of total base shear (left) and overturning moment (right) at a stack height of 6, for use in estimation of foundation costs.

may fail under different load cases on different iterations of the design. For this figure, the last load case to cause an update to the design is considered to be the controlling load case. Consequently, there is no clear boundary where between where two load cases control. However, both service and ultimate loads controlled the design for at least one point. The single turbine shutoff case appears to control more frequently when $U_0 < U_R$, while the freewheel case tends to control more frequently when $U_0 > U_R$.

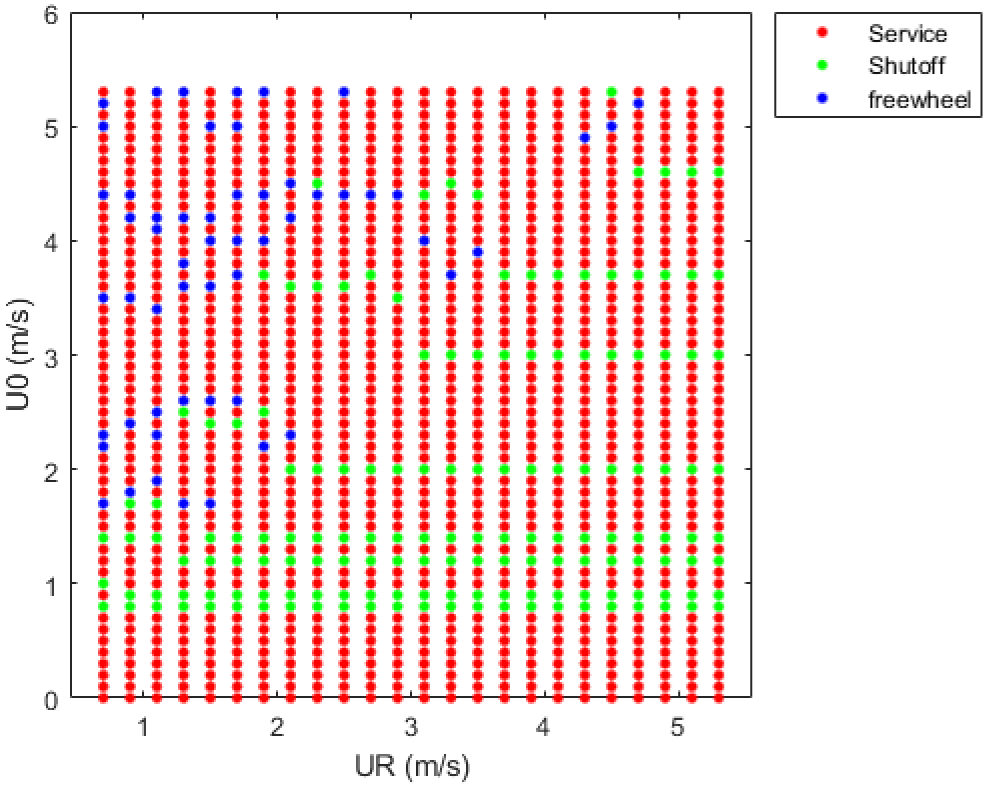

Figure 4.11: Controlling load case at each sampled point in the design space for a stack height of 6, defined as the last load case to cause an update to the structural design.

It should be noted that even if a structurally feasible superstructure design is found, it may be undesirable from a hydrodynamic standpoint. The structural sections used in this study were chosen to have minimal profile to heuristically minimize drag. However, the impacts of the superstructure on the array performance have not been studied. Thus, it may be the case that the superstructure sizing must be more strictly controlled to prevent negative hydrodynamic impacts.

Chapter 5

CONCLUSIONS

This work investigated the structural design space of vertical-axis tidal turbines using a framework that incorporates concepts from traditional civil-structural engineering to complement marine turbine design concepts. First, a load and resistance factor design framework for the turbine blades and superstructure is defined. A simplified frame model is derived to efficiently analyze the stresses and deformations in the blades. The simplified model is compared to a more detailed shell finite element model and found to slightly underestimate the stresses and deflections in the blade due to shear lag. The design framework and frame model are applied in a parametric design algorithm written in MATLAB. The parametric design algorithm is applied over a range of input parameters with loads taken from experimental and simulated hydrodynamic data.

Feasible blade designs are found for freeflow speeds up to 4.5 m/s, although this limit may be improved by a more efficient strut geometry. The blade design is mainly controlled by stress at extreme load and by normal deflections at service load, depending on the strictness of the imposed deformation limits. If the freewheel load case is not included, then the structural design is more likely to be controlled by allowable deformations or fatigue stress, though that in turn depends on the fatigue strength reduction factor. When the freewheel load case is included, the structural design becomes mostly independent of the control strategy used, because the most extreme load case occurs in an uncontrolled state. In this case, the design is dependent only on the site current speed. Feasible superstructure designs using commercially available round HSS and W14 steel sections are found for freeflow and rated speeds up to 5 m/s. The superstructure design is controlled by both service and extreme loading conditions, depending on the operating point.

5.1 Future Work

The parametric design algorithms described in this work are to be integrated into a more general techno-economic analysis framework which combines hydrodynamic analyses with structural and electrical systems designs to assess the economic viability of a turbine array for any given site and control strategy. The control and geometric parameters can be adjusted to optimize the array's levelized cost of energy. Once the turbine concept reaches the stage of development where a more detailed structural design is required, the gaps in this work regarding connection design, fatigue, and stress concentrations must be addressed.

This study uses rough estimate values for the allowable blade deformations, which affects which limit state controls the design. The actual limits of allowable blade deformation should be set by determining how far the blade can displace without significant negative impacts on hydrodynamic performance. This must be investigated through coupled fluid-structural simulations.

BIBLIOGRAPHY

[1] *Steel Construction Manual*. American Institute of Steel Construction, 14th edition, 2011.

[2] *ASCE 7-16 Minimum Design Loads and Associated Criteria for Buildings and Other Structures*. American Society of Civil Engineers, 2017.

[3] Ever J Barbero. *Introduction to Composite Materials Design*. CRC press, 2010.

[4] Gunjit S Bir, Michael J Lawson, and Ye Li. Structural design of a horizontal-axis tidal current turbine composite blade. In *International Conference on Offshore Mechanics and Arctic Engineering*, volume 44373, pages 797–808, 2011.

[5] Eun Jung Chae, Deniz Tolga Akcabay, and Yin Lu Young. Dynamic response and stability of a flapping foil in a dense and viscous fluid. *Physics of Fluids*, 25(10):104106, 2013.

[6] John O Dabiri. Potential order-of-magnitude enhancement of wind farm power density via counter-rotating vertical-axis wind turbine arrays. *Journal of Renewable and Sustainable Energy*, 3(4):043104, 2011.

[7] Mukul Dave and Jennifer A Franck. Comparison of RANS and LES for a cross-flow turbine in confined and unconfined flow. *Journal of Renewable and Sustainable Energy*, 13(6), 2021.

[8] Peter Fraenkel. Practical tidal turbine design considerations: a review of technical alternatives and key design decisions leading to the development of the seagen 1.2 mw tidal turbine. In *Ocean Power Fluid Machinery Seminar*, volume 19, pages 1–19, 2010.

[9] Chris Garrett and Patrick Cummins. The efficiency of a turbine in a tidal channel. *Journal of fluid mechanics*, 588:243–251, 2007.

[10] David M Grogan, Sean B Leen, Ciaran R Kennedy, and CM Ó Brádaigh. Design of composite tidal turbine blades. *Renewable Energy*, 57:151–162, 2013.

[11] Christopher Hoen and Vetco Aibel As. An engineering interpretation of the complex eigensolution of linear dynamic systems. In *Proceedings of International Modal Analysis Conference XXIII*, 2005.

[12] Aidan Hunt and Brian Polagye. Performance characteristics of an experimental cross-flow turbine array at high confinement. *Bulletin of the American Physical Society*, 2022.

[13] Aidan Hunt and Brian Polagye. Experimental techniques for evaluating the performance of high-blockage cross-flow turbine arrays. In *Proceedings of the 15th European Wave and Tidal Energy Conference*, 2023. (forthcoming).

[14] Laszlo P Kollar and George S Springer. *Mechanics of Composite Structures*. Cambridge university press, 2003.

[15] Benjamin Terry, Richard Wiebe, and Michael Motley. Interaction between instabilities in vertical-axis turbine blades. *Journal of Engineering Mechanics*, 149(6):04023028, 2023.